The Journal of Experimental Biology 202, 2393–2412 (1999)
Printed in Great Britain © The Company of Biologists Limited 1999
JEB2130

LOCOMOTOR FORCES ON A SWIMMING FISH: THREE-DIMENSIONAL VORTEX WAKE DYNAMICS QUANTIFIED USING DIGITAL PARTICLE IMAGE VELOCIMETRY

ELIOT G. DRUCKER* AND GEORGE V. LAUDER
Department of Ecology and Evolutionary Biology, University of California, Irvine, CA 92697, USA
*e-mail: edrucker@uci.edu

Accepted 14 June; published on WWW 25 August 1999

Summary

Quantifying the locomotor forces experienced by swimming fishes represents a significant challenge because direct measurements of force applied to the aquatic medium are not feasible. However, using the technique of digital particle image velocimetry (DPIV), it is possible to quantify the effect of fish fins on water movement and hence to estimate momentum transfer from the animal to the fluid. We used DPIV to visualize water flow in the wake of the pectoral fins of bluegill sunfish (*Lepomis macrochirus*) swimming at speeds of 0.5–1.5 $L\,s^{-1}$, where L is total body length. Velocity fields quantified in three perpendicular planes in the wake of the fins allowed three-dimensional reconstruction of downstream vortex structures. At low swimming speed (0.5 $L\,s^{-1}$), vorticity is shed by each fin during the downstroke and stroke reversal to generate discrete, roughly symmetrical, vortex rings of near-uniform circulation with a central jet of high-velocity flow. At and above the maximum sustainable labriform swimming speed of 1.0 $L\,s^{-1}$, additional vorticity appears on the upstroke, indicating the production of linked pairs of rings by each fin. Fluid velocity measured in the vicinity of the fin indicates that substantial spanwise flow during the downstroke may occur as vortex rings are formed. The forces exerted by the fins on the water in three dimensions were calculated from vortex ring orientation and momentum. Mean wake-derived thrust (11.1 mN) and lift (3.2 mN) forces produced by both fins per stride at 0.5 $L\,s^{-1}$ were found to match closely empirically determined counter-forces of body drag and weight. Medially directed reaction forces were unexpectedly large, averaging 125 % of the thrust force for each fin. Such large inward forces and a deep body that isolates left- and right-side vortex rings are predicted to aid maneuverability. The observed force balance indicates that DPIV can be used to measure accurately large-scale vorticity in the wake of swimming fishes and is therefore a valuable means of studying unsteady flows produced by animals moving through fluids.

Key words: swimming, pectoral fin locomotion, flow visualization, hydrodynamics, digital particle image velocimetry, bluegill sunfish, *Lepomis macrochirus.*

Introduction

Measuring the forces exerted by organisms on the fluids through which they move is a difficult proposition. On land, devices such as force plates allow direct measurement of the force applied by locomoting animals to the ground, but in the aquatic and aerial media, such devices are not applicable. As a result, a number of alternative approaches have been used in an effort to understand the mechanisms by which organisms propel themselves in fluids. For example, considerable effort has been expended in developing models of the process by which swimming and flying organisms generate locomotor force. Early theoretical models involved steady- or quasi-steady-state analyses that employed time-invariant lift and drag coefficients (e.g. Weis-Fogh, 1973; Blake, 1983). For swimming animals, such locomotor mechanisms have been termed ‘lift-based’ or ‘drag-based’ (for reviews, see Webb and Blake, 1985; Vogel, 1994). More recent models have elaborated a vortex theory of propulsion based on time-dependent circulatory forces rather than estimated force coefficients (Rayner, 1979a,b; Ellington, 1984b,c). Unsteady mechanisms, such as the ‘clap and fling’ (Lighthill, 1973; Weis-Fogh, 1973), take into account rotation as well as translation of the propulsor and acknowledge the complex time history of force development (see also Dickinson, 1994; Dickinson and Götz, 1996). Recently, the use of supercomputers to solve the unsteady Navier–Stokes equations for numerous grid points around a model animal has provided insights into the dynamics of locomotor force production (Carling et al., 1994, 1998; Liu et al., 1997, 1998). By deforming the model animal, a time-dependent estimate of the forces exerted on the fluid can be calculated. Despite these advances in computational approaches, however, the difficulty in empirically measuring forces exerted by freely moving

organisms on their fluid surroundings remains a major technical challenge that has limited our ability to evaluate vortex models and to understand how animals in fluids generate thrust.

The hallmark of force production in fluids is the shedding of vorticity, which reflects a transfer of momentum into the wake. Previous attempts to study biological wake vorticity have included the tracking of dye fronts, smoke and buoyant particles introduced into the fluid through which an animal moves (for reviews, see Stamhuis and Videler, 1995; Müller et al., 1997), shadowgraphic projection (McCutchen, 1977) and Schlieren imaging (Strickler, 1975). Flow visualizations of this sort provide qualitative insight into patterns of fluid movement, but are difficult to quantify especially when flow is three-dimensional. An alternative approach is to study flow in orthogonal thin (approximately two-dimensional) sections of the three-dimensional wake. Based on the original technique of Vogel and Feder (1966), researchers have developed means of illuminating particles suspended in the flow with sheets of light to investigate vorticity in the wake of flying birds (Kokshaysky, 1979), flying insects (Grodnitsky and Morozov, 1992; Brodsky, 1994; Dickinson and Götz, 1996) and swimming fish (Müller et al., 1997). Three-dimensional clouds of particles imaged with stereophotography have also been mathematically sectioned to allow analysis of the wake of birds and bats in flight (Spedding et al., 1984; Rayner et al., 1986; Spedding, 1986). These studies have provided valuable information about wake morphology and energetics, yet involved time-intensive calculations that limited the number of propulsor strokes subjected to full quantitative analysis. Additionally, unavoidable gaps in the cloud of particles within the fluid resulted in non-uniform distributions of velocity vectors in the reported flow fields.

In the present study, we employ digital particle image velocimetry (DPIV) to examine the vortex wake shed by freely swimming fish. As opposed to the manual tracking of individual particles, this sheet illumination technique involves rapid computational processing of time-variant patterns of particle images (nearly uniformly distributed), defined by pixel intensity in digitized video fields (Raffel et al., 1998). The specific objective of this study was to use the DPIV approach to quantify the forces experienced by bluegill sunfish during labriform locomotion through an analysis of the pectoral fin wake. As a first step, we described the geometry of vortex flow downstream of the pectoral fin and examined the dynamics of vortex formation over the course of the fin-stroke cycle. Unlike previous analyses of fish swimming using particle image velocimetry or particle tracking in a single plane (Stamhuis and Videler, 1995; Müller et al., 1997), we quantified flow patterns in three perpendicular planar transections of the wake using an experimental arrangement that permitted determination of the location of the fins within each flow field. Our goal was to maximize accuracy in reconstructing wake geometry and estimating locomotor forces. By collecting DPIV data in three dimensions, we were able to quantify not only locomotor lift and thrust but also laterally directed forces exerted on the fluid to obtain a full three-dimensional resolution of the reaction forces acting on a freely swimming fish.

Materials and methods

Fish

Bluegill sunfish (*Lepomis macrochirus* Rafinesque) were collected by seine from ponds in Newport Beach, CA, USA. Animals were maintained at an average temperature of 20 °C in 40 l aquaria and fed earthworms twice weekly. Eight individuals of similar size (total body length, L, 20.3±0.9 cm, mean ± S.D.) were selected for study.

Wake visualization

Sunfish swam individually at 20 °C in the working area (28 cm×28 cm×80 cm) of the recirculating freshwater flow tank described previously by Jayne and Lauder (1995). Animals were induced to hold station at three flow speeds: $0.5\,L\,s^{-1}$, at which propulsion is achieved by oscillation of the pectoral fins alone; $1.0\,L\,s^{-1}$, the speed of transition from purely labriform swimming to combined pectoral and caudal fin oscillation ($U_{p\text{-}c}$) (see Gibb et al., 1994); and $1.5\,L\,s^{-1}$, a speed at which burst-and-coast caudal fin propulsion is supplemented by intermittent pectoral fin beating. Only steady rectilinear swimming, during which the fish maintained a speed within 5 % of the flow tank's current speed, was considered for analysis. In addition, the fish was required to swim near the center of the volume of the working area; the minimum allowable distance between any wall and the pectoral fin tip was 5 cm. At lesser distances, hydrodynamic 'wall effects' (i.e. interactions of the wake with flume surfaces; Webb, 1993) were apparent from direct observation of the downstream flow. We thus ensured that only unimpeded flow structures resulting directly from movements of the fish's pectoral fins were chosen for analysis.

A digital particle image velocimetry system was developed to visualize and analyze quantitatively fluid flow in the pectoral fin's wake (Fig. 1A). Water in the flow tank was seeded at a density of $14\,mg\,l^{-1}$ with silver-coated glass spheres (mean diameter 12 μm, density $1.3\,g\,cm^{-3}$). Although slightly negatively buoyant, the spheres remained suspended in the water as a cloud of reflective particles during the course of each experiment, and particle sinking as flow traversed the working area was negligible. Light from a 3 W continuous-wave argon-ion laser was focused into a sheet 1–2 mm thick and 10 cm wide to illuminate near-fin particle motion. Two synchronized high-speed video cameras (NAC HSV-500) were used to record images of the swimming fish and its wake at $250\,fields\,s^{-1}$. One camera imaged particle reflections, while a second provided a perpendicular view of the left pectoral fin's position in relation to the laser sheet. The signals from the cameras were recorded as split-screen images, facilitating simultaneous quantification of particle motion and the location and orientation of the left fin within the flow field (Fig. 1B).

To elucidate the three-dimensional structure of the wake, a

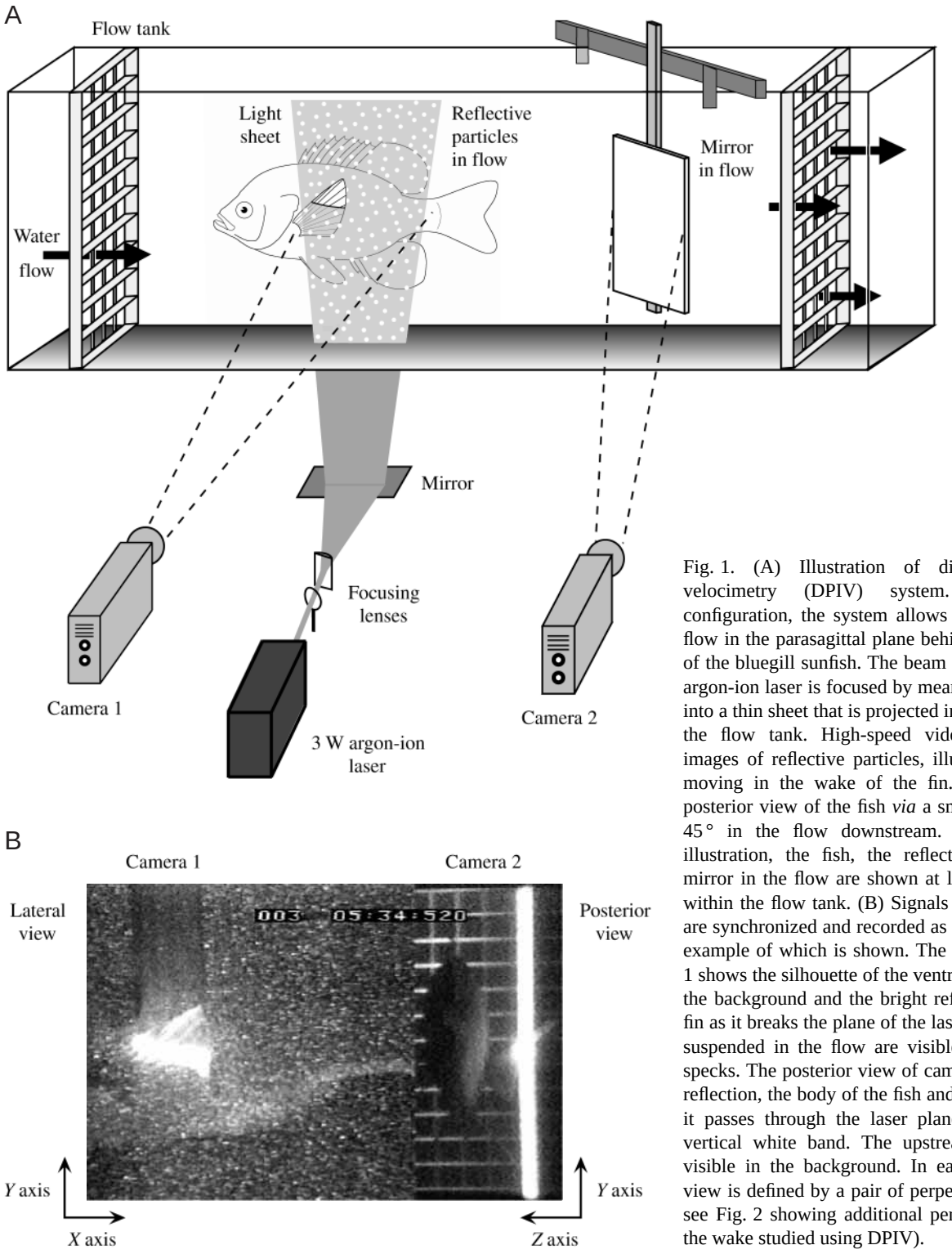

Fig. 1. (A) Illustration of digital particle image velocimetry (DPIV) system. In its depicted configuration, the system allows visualization of water flow in the parasagittal plane behind the left pectoral fin of the bluegill sunfish. The beam of light supplied by an argon-ion laser is focused by means of cylindrical lenses into a thin sheet that is projected into the working area of the flow tank. High-speed video camera 1 records images of reflective particles, illuminated by the laser, moving in the wake of the fin. Camera 2 records a posterior view of the fish *via* a small mirror mounted at 45° in the flow downstream. For the purposes of illustration, the fish, the reflective particles and the mirror in the flow are shown at larger-than-actual scale within the flow tank. (B) Signals from cameras 1 and 2 are synchronized and recorded as split-screen images, an example of which is shown. The lateral view of camera 1 shows the silhouette of the ventral margin of the fish in the background and the bright reflection of the pectoral fin as it breaks the plane of the laser light sheet. Particles suspended in the flow are visible as a cloud of white specks. The posterior view of camera 2 shows, in mirror reflection, the body of the fish and the left pectoral fin as it passes through the laser plane, seen on edge as a vertical white band. The upstream collimator grid is visible in the background. In each case, the plane of view is defined by a pair of perpendicular axes (*X*, *Y*, *Z*; see Fig. 2 showing additional perpendicular sections of the wake studied using DPIV).

series of front-surface mirrors was used to align the light sheet, in separate experiments, in three orthogonal planes: frontal (*XZ*), parasagittal (*XY*) and transverse (*YZ*) (Fig. 2). Thus, data presented below for perpendicular light sheets were not collected simultaneously. For each laser orientation, flow around the fin was examined in a variety of planar sections ranging from the fin base to the distal fin tip. Data presented here are from planes positioned approximately half-way along the span of the abducted pectoral fin, the location at which wake vortices were best defined. DPIV data were collected from five fish to establish general vortex flow patterns. Fifty-five pectoral fin strokes performed by two of these individuals

at $0.5\,L\,s^{-1}$ were selected for a detailed analysis of the wake produced by slow labriform swimming. In total, 143 image pairs were extracted from these strokes and analyzed quantitatively to characterize planar flow patterns near the fin over the course of the fin-beat cycle. An additional 40 fin beats and 117 image pairs were examined at 1.0 and $1.5\,L\,s^{-1}$ to allow quantification of vortex flow at higher speeds.

Quantitative image analysis

After review of video tapes to select scenes of steady swimming, pairs of successive video images (separated by the framing period Δt=4 ms) were digitized at eight bits per pixel (grayscale) and downloaded to hard disk. The portion of each digital field available for processing (i.e. containing particle images) was 440 horizontal × 480 vertical pixels. DPIV recordings were quantitatively evaluated by means of two-frame cross-correlation (Raffel et al., 1998). Image interrogation was performed computationally using a 20×20 grid (Insight v. 3.0 software, TSI Inc., St Paul, MN, USA). The displacement of particle images over Δt was analyzed by cross-correlation to yield two-dimensional flow fields, typically 6–8 cm on each side, each consisting of 400 uniformly distributed water velocity vectors. Analysis of these vector diagrams at selected times during the fin beat, and in different perpendicular planes, allowed reconstruction of the time course of development and three-dimensional geometry of the pectoral fin's wake. Reconstruction of the wake from non-simultaneous orthogonal flow fields (Fig. 2) assumes low among-stroke (intra-individual) variation in the three-dimensional pectoral fin kinematics of *Lepomis macrochirus*, as documented by Gibb et al. (1994).

Post-processing of DPIV data began with validation of the velocity vectors. A dynamic mean value algorithm was used to reject each vector whose velocity markedly exceeded the average velocity of its eight nearest neighbors (Raffel et al., 1998). Validated vectors that clearly misrepresented the actual flow were detected by visual inspection of each vector field and were deleted manually. When they occurred, such erroneous vectors were at the edges of the data field and near the fish's fin (i.e. when light-sheet images included the fin itself), whose velocity (both magnitude and direction) most often differed from that of the surrounding fluid. Gaps in the vector field arising from validation were filled by interpolation in a 3×3 vector neighborhood (least-squares fit estimate). The overall measurement accuracy of the DPIV system was assessed by comparing the average free-stream velocity calculated by cross-correlation with that determined by tracking individual particles in the video record. In 20 fin beats examined, the DPIV estimation of velocity was within 5 %, on average, of the true velocity.

Calculated velocity vectors were used to compute derivative and integral quantities of hydrodynamic significance. Vorticity (ω), a measure of fluid angular velocity, was calculated to illustrate rotation in the local flow field. For the three perpendicular laser planes, vorticity components were computed by Datashow software (TSI Inc.) according to:

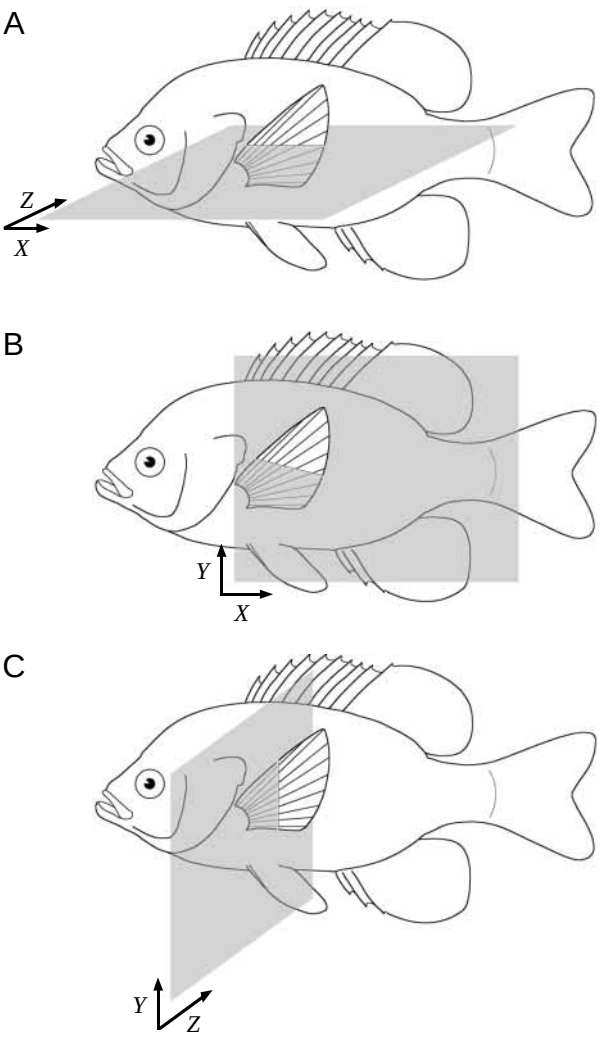

Fig. 2. Illustration of three perpendicular planes illuminated by laser light for DPIV flow visualization. Flow patterns in the wake of the left pectoral fin were examined in planes positioned approximately half-way along the span of the abducted fin. (A) Frontal (*XZ*). (B) Parasagittal (*XY*). (C) Transverse (*YZ*). Axis pairs define the planes of analysis, but not the specific origin of any coordinate system. In separate experiments, the frontal plane was imaged ventrally using a video camera mounted beneath the flow tank, the parasagittal plane was video-taped from the left (see Fig. 1), and the transverse plane was viewed from a posterior perspective.

$$\vec{\omega} = \left(\frac{\partial w}{\partial Y} - \frac{\partial v}{\partial Z}, \frac{\partial u}{\partial Z} - \frac{\partial w}{\partial X}, \frac{\partial v}{\partial X} - \frac{\partial u}{\partial Y} \right), \quad (1)$$

where u, v and w are the velocity components parallel to the X, Y and Z flow-field axes (Fig. 2) (Lighthill, 1986). The total strength of a vortex in a given plane was measured in terms of circulation, Γ, the line integral of the tangential velocity component $\vec{V}$ about a curve C enclosing the vortex (Batchelor, 1967):

$$\Gamma = \oint_C \vec{V} \cdot d\vec{l}, \quad (2)$$

where $d\vec{l}$ is the incremental path element vector. A custom-designed computer program was used to evaluate equation 2. The user defined a circular integration path C around each vortex center interactively upon the 20×20 vector matrix. Velocities at points on C were determined by linear interpolation from the closest four neighboring vectors in the matrix, and the tangential components were summed around C. Γ was calculated at increasing integration path radii (increment 0.2 cm) until an asymptotic value, representing the vortex's total circulation, was attained (Willert and Gharib, 1991).

Flow-field geometry

Velocity vector maps were displayed graphically, and the average free-stream velocity U_f (i.e. the speed of the current distant from the wake) was subtracted from each vector in the frontal and parasagittal matrices to reveal vortical flow structures. Since the current passed perpendicularly through the transverse light sheet (Fig. 2C), it was not necessary to subtract U_f in this plane. At swimming speeds greater than $0.5\,L\,s^{-1}$, increased flow normal to the transverse light sheet resulted in out-of-plane loss of particle images over Δt, which greatly limited the possibility of valid correlation peak detection. Accordingly, vortex geometry at 1.0 and $1.5\,L\,s^{-1}$ was analyzed in frontal and parasagittal slices of the wake only.

To compare the morphology of vortices shed by the pectoral fin with theoretical vortical structures, velocity gradients across the wake were examined. For each orthogonal laser plane, the pair of axes defining the flow field (X–Z, X–Y or Y–Z) was rotated through an angle ψ, measured between the horizontal axis of the vector map and the longitudinal axis of the wake structure of interest (see Fig. 5C). Thus, the original perpendicular components of each velocity vector in a two-dimensional slice through the wake were transformed to components oriented along the rotated axes (X', Y', Z') (see equation 2 in Spedding, 1986). These new components of velocity were plotted against position along the wake's rotated major axes to yield flow velocity profiles. From such profiles, meristic variables describing the linear dimensions of the wake were measured (see Results).

Force measurements

To evaluate the balance of horizontal and vertical forces acting on the sunfish during constant-speed pectoral fin locomotion, total body drag (D) and weight (F_g) were determined empirically and compared with propulsive forces calculated from DPIV data. Sunfish were lightly anesthetized with tricaine methanesulfonate ($0.3\,g\,l^{-1}$ buffered with KOH) to eliminate movement of the body or fins and to allow a loop of suture (6-0 gauge silk) to be passed around the dentary symphysis and upper lip. The use of live animals allowed the natural mucus covering on the body to remain intact. Two anesthetized fish (L=21–22 cm), used previously for DPIV experiments, were towed individually from a force transducer suspended in the flow tank at a current speed of $0.5\,L\,s^{-1}$ to measure D. To determine F_g, eight sunfish, including four used for the DPIV experiments, were anesthetized and weighed under water to the nearest 0.01 g using a pan balance.

Propulsive forces on the pectoral fins arising from bound circulation were inferred from near-fin circulation of vortices in the wake. This inference is justified by the equivalence in magnitude of bound and shed Γ, according to Kelvin's theorem, during the impulsive start of a hydrofoil (Milne-Thomson, 1966; Dickinson, 1996) such as that observed during pectoral fin abduction. Locomotor force experienced by the fin was calculated as the reaction of the wake's momentum flow following Dickinson and Götz (1996). The momentum (M) of a vortex ring shed into the wake (see Results) may be estimated from a planar section using:

$$M = \rho\Gamma A\,, \tag{3}$$

where ρ is water density ($1000\,kg\,m^{-3}$ at 20 °C) and A is the projected area of the vortex ring onto the laser plane. In equation 3, Γ and A were measured at the end of the complete fin-stroke cycle. For each pectoral fin, the instantaneous force (F) associated with the vortex wake (Milne-Thomson, 1966) is given by:

$$F = dM/dt\,. \tag{4}$$

Thus, the time-averaged total locomotor force $\bar{F}$ can be calculated from:

$$\bar{F} = \rho\Gamma A/T\,. \tag{5}$$

At $0.5\,L\,s^{-1}$, a speed at which propulsive force is generated entirely by the pectoral fins, T was taken as the fin-stroke period, the sum of fin downstroke duration (T_d), fin upstroke duration (T_u) and a brief kinematic pause period (Gibb et al., 1994). For higher speeds ($U_{p\text{-}c}$ and above), at which pectoral fin oscillations are intermittent and the pause period is highly variable, T was taken as the sum of T_d and T_u.

For each orthogonal velocity vector field, the angle ϕ between the horizontal axis and the mean orientation of the central water jet of the vortex ring was measured. The force arising in reaction to the wake of the left pectoral fin was then resolved into its perpendicular components running parallel to the X, Y and Z axes. The upstream component of force acting on the fin F_x (thrust) was calculated independently in the frontal and parasagittal planes as $\bar{F}\cos\phi$, and the upward component F_y (lift) was calculated from the parasagittal and transverse planes as $\bar{F}\sin\phi$. These values were doubled to account for the action of both fins and to allow an estimate of the total thrust and lift experienced by the whole animal over the course of the fin stroke. The medially directed component of the reaction force on each fin F_z was calculated from the frontal and transverse planes as $\bar{F}\sin\phi$ and $\bar{F}\cos\phi$, respectively (Fig. 2; see equations 9, 10 in Spedding, 1987).

Results

Wake measurements at 0.5 L s^{-1}

Vortex flow patterns

Labriform locomotion in *Lepomis macrochirus* involves an oscillatory cycle of (1) anteroventral fin movement

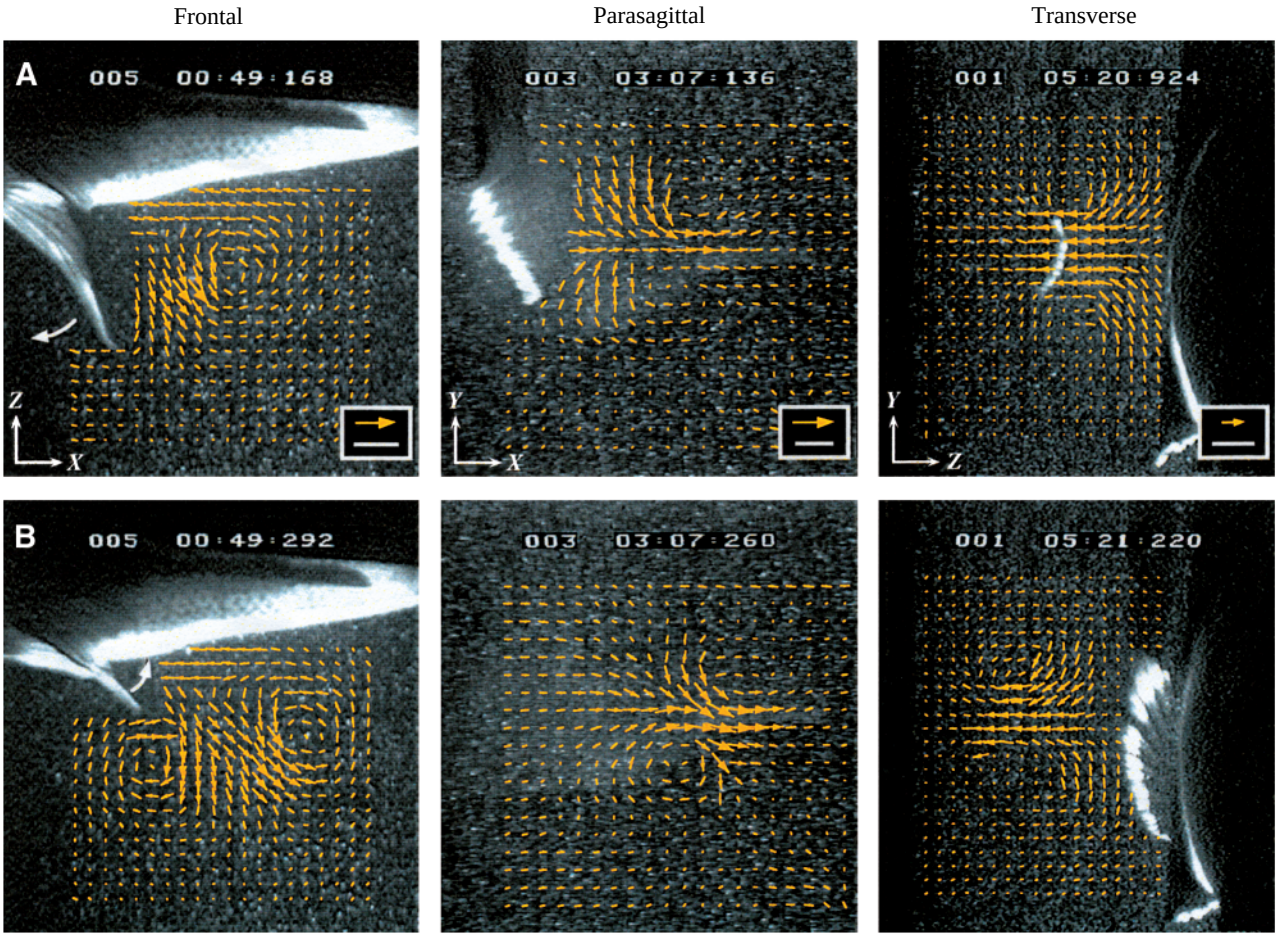

Fig. 3. Water velocity vector fields calculated for orthogonal planar sections of the pectoral fin wake (see Fig. 2) during swimming at $0.5\,L\,s^{-1}$. Frontal plane: ventral view, anterior and upstream to the left. Parasagittal plane: left lateral view, anterior and upstream to the left. Transverse plane: posterior view showing the left side of body and the left fin; free-stream flow passes perpendicularly through the plane of the page towards the viewer. Flow patterns are shown at the time of (A) the stroke reversal, following fin downstroke in the direction of the upper curved arrow, and (B) mid to late upstroke in the direction of the lower curved arrow. The last three digits in the numerical code in each panel denote time (in ms). Mean free-stream flow velocity ($10.5\,cm\,s^{-1}$ from left to right) has been subtracted from the frontal- and parasagittal-plane vector matrices to reveal wake structure. Note the spanwise component of flow in the frontal plane. By the middle to end of the upstroke, discrete pairs of counterrotating starting and stopping vortices are visible in each plane, each with a central jet of relatively high-velocity flow (B). Scales: arrow, $20\,cm\,s^{-1}$; bar, 1 cm.

(downstroke), (2) rotation of the fin around its long axis at the end of downstroke (stroke reversal, or fin 'flip'), (3) posterodorsal fin movement (upstroke), and (4) a kinematic pause period during which the fin is held flush against the body. DPIV flow fields reveal that, at $0.5\,L\,s^{-1}$, the downstroke and stroke reversal are the primary generators of wake vorticity. During the downstroke, a free starting vortex is seen immediately downstream of the dorsal margin of the pectoral fin in the parasagittal and transverse planes (Fig. 3A, upper vortices; Fig. 4, *P*1, *T*1). At the end of the downstroke, and as the stroke reversal begins, a stopping vortex becomes visible near the ventral edge of the fin (Fig. 3A, lower vortices; Fig. 4, *P*2, *T*2). Within the frontal plane, only a single vortex is observable during the downstroke, but a second vortex appears as the fin rotates and begins to return towards the body (Figs 3A,B, 4, *F*1, *F*2). In all three planes, completion of the stroke cycle results in a discrete pair of counterrotating vortices introduced into the wake. Between each vortex pair, and strengthened by the rotational fluid motion, is a jet flow oriented posteriorly (downstream), ventrally and laterally (Fig. 3B). During the downstroke, the developing jet flow has a distinct spanwise component: velocity vectors near the fin are oriented parallel to the fin rays (Fig. 3A, frontal). Water encountering the anterior fin margin early in the stroke is drawn posterolaterally along the fin to contribute to vortex *F*1.

Plots of vorticity components calculated from planar velocity fields illustrate the opposite-sign rotation of the vortex pair in each perpendicular plane (Fig. 4). The observed vortices are consistent with slices through a toroidal structure and indicate that each fin sheds one complete vortex ring per stroke cycle at $0.5\,L\,s^{-1}$ (see Fig. 8E). A hierarchical analysis of variance (ANOVA) with paired vortices nested within laser

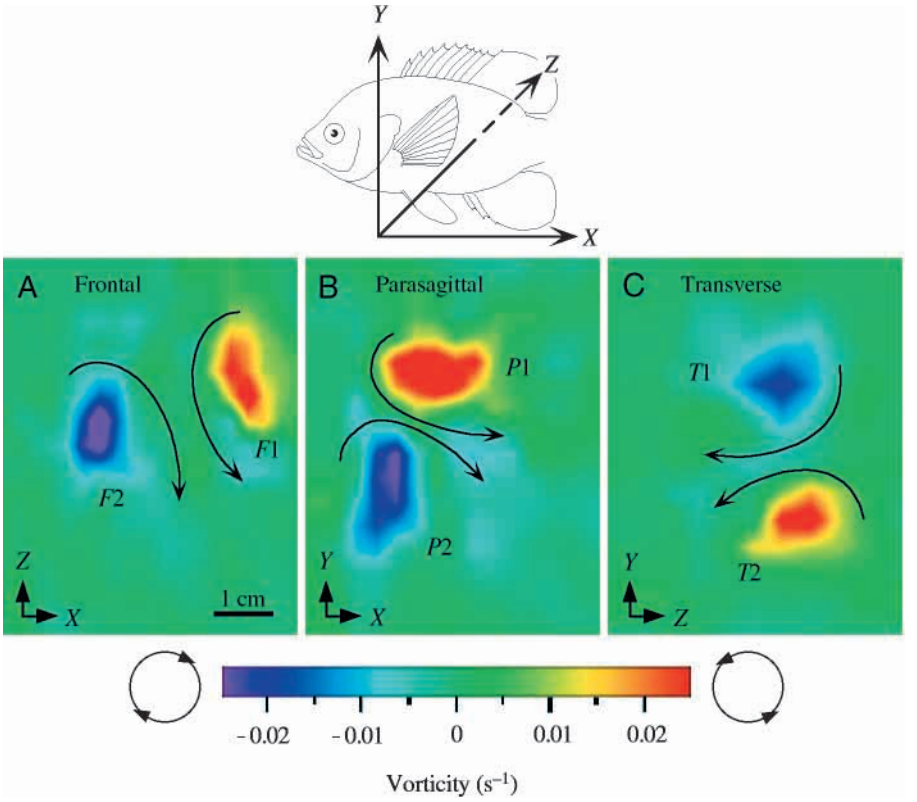

Fig. 4. Fluid vorticity components in three perpendicular wake planes (A–C) during swimming at $0.5\,L\,s^{-1}$. Vorticity posterior to the left pectoral fin is shown at the time of completion of the fin-beat cycle (orientation and approximate position of flow planes with respect to the fish are indicated by the axes at the top; see Fig. 2). Red/orange coloration represents positive vorticity or counterclockwise fluid rotation, while blue/purple colors indicate negative or clockwise rotation. Green regions reflect a lack of rotational motion. Arrows between the pairs of counterrotating vortices show the direction of the fluid jet present in all three planes (see velocity vectors in Fig. 3B). This pattern of vortex flow, generated during the downstroke, indicates the production of a single toroidal vortex loop in the wake. *F*1, *P*1, *T*1, downstroke starting vortices; *F*2, *P*2, *T*2, downstroke stopping vortices. The scale bar applies to A–C.

plane orientation indicated that circulation magnitude does not differ significantly between starting and stopping vortices (d.f.=3 between vortices within planes; P=0.65). The average of clockwise and counterclockwise vortex strength (Table 1, Γ) was therefore used in each plane for calculations involving total ring circulation (equations 3, 5). Vortex ring momentum angle (Table 1, ψ), the angle of inclination of the line connecting the two vortex centers, became acute within 200–300 ms of the start of the fin beat (Figs 3, 4). Mean momentum angles measured at the end of the stroke in each flow plane differed significantly from one another (Bonferroni multiple-comparison test at α=0.0167), indicating an oblique orientation of the vortex ring and its central water jet in space.

Velocity profiles and vortex dimensions

Both theory (Milne-Thomson, 1966) and experimental studies of man-made vortex rings in fluid (Maxworthy, 1977; Raffel et al., 1998) provide details of wake morphology with

Table 1. *Vortex ring measurements from perpendicular flow-field sections of the wake during swimming at 0.5* L *s*$^{-1}$

	Flow-field plane			
Measurement	Frontal	Parasagittal	Transverse	*F*
Ring momentum angle ψ (degrees)	23.04±3.24	39.70±5.06	81.02±3.47	64.5*** (16)
Jet angle ϕ (degrees)	–54.74±3.78	–49.49±6.38	–8.35±2.56	36.1*** (16)
Ring radius $R\times10^2$ (m)	1.91±0.08	1.61±0.09	1.78±0.07	3.2 (18)
Ring area $A\times10^4$ (m^2)	11.57±0.96	8.29±0.89	10.22±0.89	2.9 (18)
Mean vortex core radius $R_o\times10^2$ (m)‡	1.06±0.11	1.13±0.09	1.16±0.13	0.21 (18)
Mean vortex circulation $\Gamma\times10^4$ (m^2 s^{-1})‡	60.81±3.94	42.59±10.10	60.33±8.11	1.6 (7)
Ring momentum $M\times10^5$ (kg m s^{-1})	711.04±140.98	352.29±61.19	616.43±63.22	3.8 (12)

All measurements made at the end of the stroke cycle and are reported as mean ± S.E.M.; N=3–8 per plane.

For ψ and ϕ, positive and negative values indicate, respectively, angles above and below the horizontal.

‡Average magnitude of measurements for clockwise and counterclockwise vortices within each plane. Nested analyses of variance revealed no significant differences between vortices within planes (see text).

F-statistics from one-way analyses of variance conducted on variables measured in each of three flow-field planes. d.f. = 2 among planes; degrees of freedom within planes are shown in parentheses.

Significance was assessed at the Bonferroni-adjusted α=0.0071.

***P<0.001.

L, total body length.

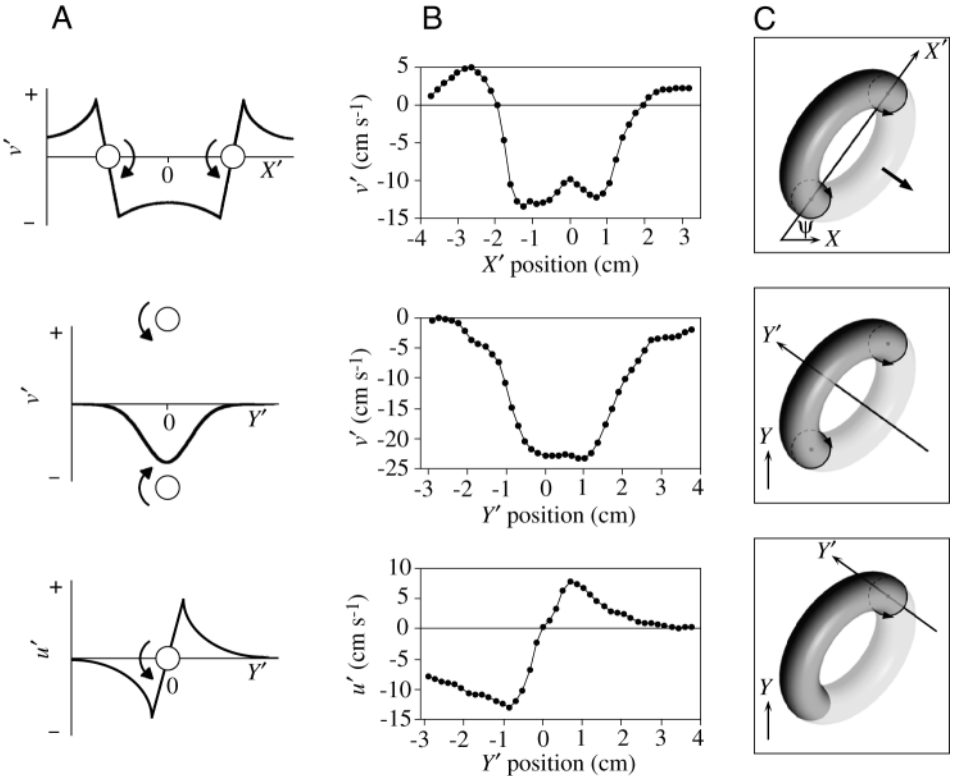

Fig. 5. Velocity profiles for vortex rings. (A) Theoretically predicted velocity distributions across a planar section of an axisymmetric vortex ring (Milne-Thomson, 1966). Vortex cores in solid-body rotation are indicated by paired circles; arrows signify the direction of induced flow rotation. Top panel: X' is the ring's longitudinal axis, which traverses the two vortex core centers. Middle panel: Y' is the central axis of the ring, perpendicular to X'. Bottom panel: Y' is the line extending across the counterclockwise vortex core parallel to the ring's central axis. Components of velocity parallel to X' and Y' are u' and v', respectively; v' is negative in the direction of the central fluid jet. (B) Empirically determined velocity profiles for sunfish vortex rings in the parasagittal plane produced at $0.5\,L\,s^{-1}$. X'=0 is the point equidistant between the two vortex core centers; Y'=0 is the point of intersection with the X' axis. The similarity between the theoretical and empirical profiles supports the existence of a roughly symmetrical vortex loop in the wake. (C) Illustration of X' and Y' axes, rotated with respect to horizontal X and vertical Y axes, within a parasagittal section of the proposed vortex loop (see Discussion). ψ, momentum angle. The bold arrow indicates the direction of the central fluid jet of the wake.

which the sunfish's wake may be compared. Fig. 5A shows three flow velocity distributions across planar sections of an ideal, axisymmetric vortex ring. For the purpose of illustration, these distributions are shown for the parasagittal (XY) plane, within which are the rotated X' axis, the longitudinal axis of the ring traversing both vortex core centers, and the perpendicular Y' axis. The components of velocity parallel to X' and Y' are defined as u' and v', respectively. Thus, in Fig. 5A, the top flow profile $v'(X')$ illustrates variation in the water velocity component perpendicular to the longitudinal axis of the ring at positions along X', the middle profile $v'(Y')$ is the distribution of velocity oriented along the ring's central axis, and the bottom profile $u'(Y')$ depicts the relationship between velocity parallel to X' and position along the perpendicular axis traversing a single vortex core. In each theoretical profile, velocities attain their greatest magnitude at the edges of the vortex cores in solid-body rotation and in the region between the vortices, reflecting the ring's central water jet. Examples of velocity gradients determined empirically from pectoral fin flow data at $0.5\,L\,s^{-1}$ in the parasagittal plane are given in Fig. 5B.

Velocity gradients across the sunfish's wake also serve to define the geometry of the interior of the vortex ring. From profiles of $v'(X')$ in the parasagittal plane, and corresponding profiles in the frontal and transverse planes, vortex ring radius R was taken as half the distance between the points of intersection of the plotted curve with the long axis of the ring (following Spedding, 1986). Measurements of R in the three perpendicular planes differed by no more than 16 % (2.9 mm) on average at $0.5\,L\,s^{-1}$, and the vortex ring was therefore assumed to be circular in projected area ($A=\pi R^2$). Neither R nor A demonstrated a significant dependence upon the orientation of the flow-field plane (Table 1). Vortex core radius R_o, an indication of ring thickness, was measured in each plane from profiles of the type shown at the bottom of Fig. 5B as half the distance along Y' between the maximum and minimum values of u' (following Spedding, 1986; Müller et al., 1997). A hierarchical ANOVA with paired vortices nested within laser plane orientation indicated that R_o does not differ significantly between starting and stopping vortices (d.f.=3 between vortices within planes; P=0.50). Averages of clockwise and counterclockwise vortex core radii in each plane are reported in Table 1. On the basis of measurements pooled across the three planes, the vortex ring at the end of the stroke period ($0.5\,L\,s^{-1}$) had a mean area of 10.2 cm^2 with R=1.8 cm and mean R_o=1.1 cm.

Force balance

Hydrodynamic forces acting on the bluegill sunfish during pectoral fin swimming at $0.5\,L\,s^{-1}$ are summarized in Table 2. Each component of locomotor force calculated from the wake depended directly upon the orientation of the central momentum jet of the vortex ring. Mean jet orientation varied significantly with flow-field plane (Table 1, ϕ), a result that Bonferroni multiple-comparison tests (α=0.0167) attributed to the marked difference in ϕ between the transverse plane and

Table 2. *Locomotor force components calculated from perpendicular flow fields at 0.5* L s^{-1}

	Flow-field plane					
Force component‡	Frontal	Parasagittal	Transverse	t_1	t_2	t_3
F_y (mN)	–	1.85±0.47	1.46±0.30	0.77 (10)	–0.36 (18)	–
F_z (mN)	6.59±1.77	–	7.23±0.95	–0.57 (10)	–	–
F_x (mN)	7.36±1.29	3.76±1.59	–	1.62 (8)	–	0.62 (16)

‡Average force over stroke cycle duration calculated using equation 5.

All forces are reported as means ± S.E.M.; N=5–7 per plane. Positive values of F_y, F_z and F_x indicate, respectively, upward-, medially and forward-directed reaction forces on each pectoral fin.

t-tests compare components of force estimated independently from two planes (t_1), total lift $2F_y$ (2× pooled mean from parasagittal and transverse planes ± S.E.M.=3.24±0.51 mN) with submerged body weight (mean ± S.E.M.=3.37±0.31 mN; N=8) (t_2), and total thrust $2F_x$ (2× pooled mean from frontal and parasagittal planes ± S.E.M.=11.12±2.27 mN) with measured body drag (mean ± S.E.M.=10.58±0.50 mN; N=8) (t_3). Degrees of freedom are tabulated in parentheses.

Significant differences were not detected at the Bonferroni-adjusted α=0.0167.

L, total body length.

the other planes. Since force arises from changes in fluid momentum, it was necessary to quantify, for each plane, the component of momentum carried into the wake by the vortex ring as well as the period of locomotor force production. Average ring M exhibited considerable variation both among and within flow-field planes; significant differences among planes were not detected (Table 1). The pectoral fin-beat period averaged 0.83±0.04 s (mean ± S.E.M., N=18) at 0.5 L s^{-1}.

Independent estimates of F_x from frontal- and parasagittal-plane flow data were not significantly different, averaging 5.56±1.14 mN per fin (mean ± S.E.M., N=10). Similar agreement was observed for F_y obtained from the parasagittal and transverse planes (pooled mean ± S.E.M.=1.62±0.25 mN, N=12) (Table 2). To account for the contributions of both left and right pectoral fins, mean values of F_x and F_y were doubled to yield the total reaction forces on the animal. These wake-derived forces were very closely balanced by empirically determined counter-forces. The average total thrust force (11.12 mN) and lift force (3.24 mN) calculated from the wake did not differ significantly from the respective resistive forces of body drag, as measured from towing experiments (10.58 mN) and submerged body weight (3.37 mN) (Table 2).

F_z pooled across planes was 6.96±0.88 mN per fin (mean ± S.E.M., N=12). This medially directed component of force, assumed to cancel on opposite sides of the animal, averaged 125 % of F_x per fin and exceeded mean F_y by a factor of greater than four.

Speed effects

As viewed in the parasagittal plane, the wake at 1.0 L s^{-1} consisted of a downstroke vortex pair (Fig. 6B, $P$1, $P$2), analogous to that formed at 0.5 L s^{-1} (Fig. 4B), and a new upstroke vortex pair created as the fin adducts (Fig. 6B, $P$3, $P$4). Between each pair, a region of linear jet flow was observed. The parasagittal flow-field data therefore reflect the production of two (at least partially complete) vortex rings over the course of the fin-beat cycle (see Fig. 9C). The downstroke ring, like that measured at 0.5 L s^{-1}, lay at an acute angle (ψ=75.1±5.8 °, mean ± S.E.M., N=6); the upstroke ring was approximately vertical in orientation (96.7±9.1 °, N=6) with a downstream-directed momentum jet. At 1.5 L s^{-1}, clockwise circulation produced in the parasagittal plane at the end of the downstroke and at the beginning of the upstroke coalesced into a single intense vortex (Fig. 6D, $P$2+$P$3). The strength of this combined vortex (Γ=–0.0053±0.0007 m^2 s^{-1}, mean ± S.E.M., N=5) was very nearly equal to the sum of mean Γ for $P$2 (–0.0026 m^2 s^{-1}) and $P$3 (–0.0033 m^2 s^{-1}) shed individually at 1.0 L s^{-1}. For the purposes of calculation (equations 3, 5), vortex ring strength at 1.5 L s^{-1} was taken as the average of Γ magnitude for $P$1 (downstroke ring) or $P$4 (upstroke ring) and half the magnitude of Γ for $P$2+$P$3. The downstroke vortex ring at the fastest swimming speed studied had a rather shallow momentum angle (26.9±5.1 °, N=5), whereas for the upstroke ring this angle was obtuse (132.2±10.5 °, N=5), resulting in a fluid jet oriented downstream and slightly above the horizontal (Fig. 6D).

Concurrent with the development of $P$1 and $P$2 at both 1.0 and 1.5 L s^{-1} was the appearance of paired vortices in the frontal plane (Fig. 6A,C, $F$1, $F$2). However, no additional vorticity was detected in the frontal plane during the upstroke. Over the complete range of swimming speeds studied, the orientation of the frontal vortex pair changed little (cf. Figs 4, 6), but ring radius measured from this plane declined steadily (Fig. 7A). Downstroke ring R and total ring Γ determined in the parasagittal plane showed a less direct relationship with speed (Fig. 7B,C). The total fluid momentum injected into the wake by each pectoral fin stroke, and the associated thrust force, increased up to the pectoral–caudal gait transition speed, and above $U_{p\text{-}c}$ plateaued or declined slightly (Fig. 7D,E).

Discussion

Vortex ring production by paired fins

Three lines of evidence obtained from DPIV experiments support the generation of a vortex ring wake by the pectoral fins of bluegill sunfish. First, the simplest geometric

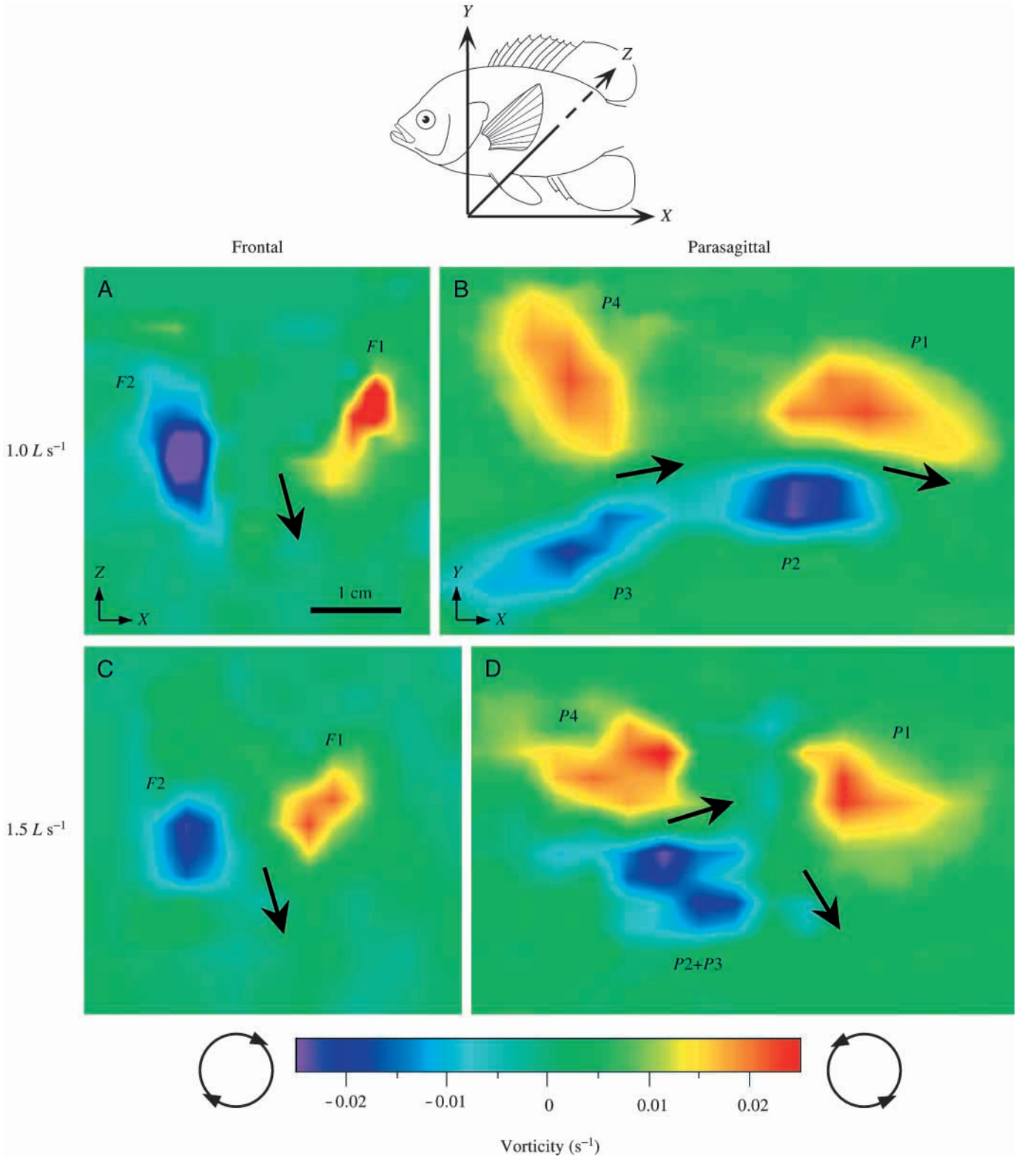

Fig. 6. Vorticity components in perpendicular planes during swimming at 1.0 and 1.5 $L\,s^{-1}$. Wake planes are located posterior to the left pectoral fin (see axes at top and Fig. 2) and illustrate flow patterns at the end of the fin-beat cycle. Note the appearance at 1.0 $L\,s^{-1}$ of an upstroke vortex pair in the parasagittal plane (B, *P*3 and *P*4) not observed at 0.5 $L\,s^{-1}$ (cf. Fig. 4B). In the frontal plane (A,C), a single pair of vortices arising from the downstroke (*F*1 and *F*2) remains the only major vortex flow detected. At 1.5 $L\,s^{-1}$, clockwise vorticity produced by the downstroke and upstroke in the parasagittal plane coalesces into a single structure (D, *P*2+*P*3). The central fluid jets generated by each half-stroke are represented by bold arrows. *P*3, upstroke starting vortex; *P*4, upstroke stopping vortex; *P*2+*P*3, combined downstroke stopping and upstroke starting vortex. Other abbreviations as in Fig. 4. The scale bar applies to A–D.

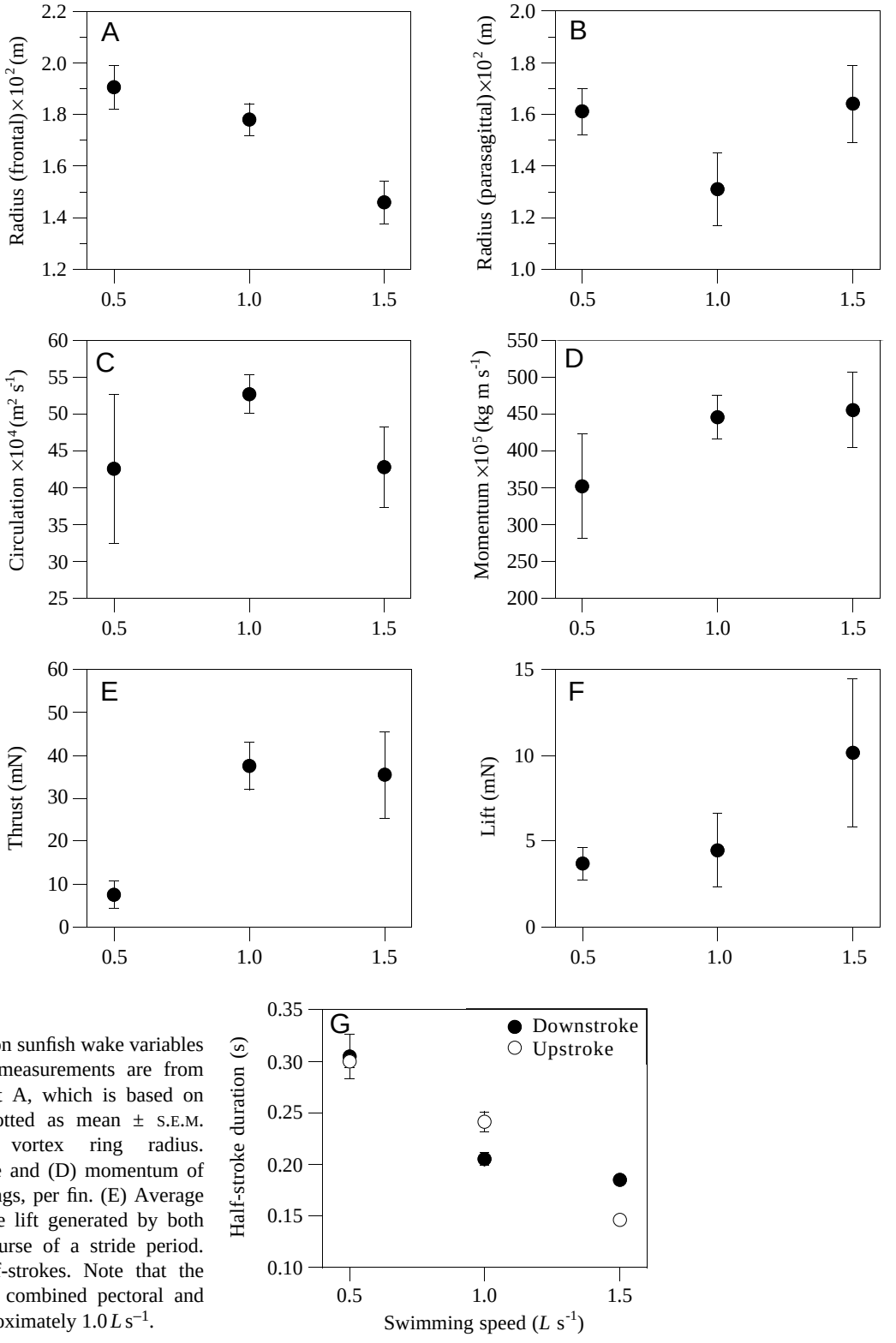

Fig. 7. Effects of swimming speed on sunfish wake variables and fin-stroke timing. All wake measurements are from parasagittal-plane flow data except A, which is based on frontal-plane data. Values are plotted as mean ± S.E.M. (N=3–10). (A,B) Downstroke vortex ring radius. (C) Summed circulation magnitude and (D) momentum of downstroke and upstroke vortex rings, per fin. (E) Average forward thrust and (F) net positive lift generated by both pectoral fins together over the course of a stride period. (G) Duration of pectoral fin half-strokes. Note that the transition from purely pectoral to combined pectoral and caudal fin swimming occurs at approximately 1.0 L s^{-1}.

interpretation of paired, counterrotating vortices produced concurrently in each of three perpendicular flow fields (Fig. 3) is the transection of a three-dimensional vortex tube closed upon itself. Helmholtz's theorem, a conservation law governing the behavior of fluids (Milne-Thomson, 1966, p. 169), in fact requires that vortex filaments either arise and terminate on solid boundaries (in this case, the fin or flank of the animal) or form a closed vortex ring. Second, Helmholtz's theorem states that the magnitude of circulation is equal around any two circuits (i.e. cross-sectional paths) along a vortex tube

(Fung, 1990, p. 91). The lack of a significant difference in Γ both between vortices within each plane and among different planes (Table 1) satisfies the theoretical condition for a vortex ring. Third, the resemblance between the pectoral-fin wake profiles measured for sunfish (Fig. 5B) and the velocity gradients for ideal, axisymmetric vortex rings (Fig. 5A) suggests the production of a grossly symmetrical vortex toroid. Flow profiles similar to those in Fig. 5B have been defined for thin parasagittal sections of the wake of birds (e.g. Spedding et al., 1984; Spedding, 1986) and demonstrated in frontal sections of the wake of a fish's tail (Müller et al., 1997), supporting the existence of the vortex ring wake behind animals moving through fluids.

Although few significant differences in ring morphology were detected across planes (Table 1), asymmetries in the wake undoubtedly exist. R measured at $0.5\,L\,s^{-1}$ from the parasagittal plane, for instance, was 0.17–0.30 cm less on average than that from the other planes, raising the possibility that the vortex ring is shed in a slightly elliptical, rather than circular, configuration. Possible deformation of the ring at higher swimming speeds is also suggested by minor discrepancies between planar estimates of R (Fig. 7A,B). Vortices visualized in planar sections of the wake appear approximately circular (Fig. 3), yet regions of concentrated vorticity do not (Fig. 4), indicating that flow velocities are not uniform throughout the wake structure. Further geometrical asymmetry was observed in the orientation of the ring's momentum jet. In a perfectly symmetrical vortex ring, the central momentum flow extends perpendicularly from the ring plane such that the momentum angle and the jet angle are complementary. For sunfish, the sum of the magnitudes of these angles does approximate 90° in the parasagittal and transverse planes, but consistently falls short of 90° in the frontal plane (by an average of 12°: Table 1; Fig. 3B, frontal). This divergence from the expectations of an ideal ring is probably related to the necessity of generating a strong downstream component of jet flow to experience forward thrust as a reaction.

There is no *a priori* reason to expect the sunfish to produce a strictly symmetrical ring, as observed in studies of non-biological vortex flows (e.g. ejection of fluid by a piston from a circular nozzle; see Maxworthy, 1972, 1977; Didden, 1979; Raffel et al., 1998). The wake behind a swimming animal is the product of rapidly accelerating and reciprocating hydrofoils which are asymmetric in shape, change over time in contour and surface area, and move in a complex three-dimensional manner. Unsteady flows of this type are highly unlikely to resemble more controlled, man-made wakes. The pectoral fin of bluegill sunfish, as in most teleost fishes, possesses a relatively stiff leading edge that is under direct muscular control during locomotion (Gosline, 1971; Gibb et al., 1994; Westneat, 1996; Drucker and Jensen, 1997). In contrast, the posterior fin margin appears to be mostly passive during the fin beat at low speeds (Gibb et al., 1994). Differing mechanical properties of the anterior and posterior fin margins, coupled with complex fin motion, may generate a somewhat elliptical vortex ring. The wake of the bluegill sunfish may be most accurately compared with a 'vortex loop' (Dickinson and Götz, 1996), a closed vortex tube obeying the required physical conservation laws but possessing a non-circular projected area and lacking an internal plane of symmetry.

On the basis of patterns of fin motion and the observed fluid flows quantified using DPIV, we suggest the following interpretation of vortex wake dynamics during the fin-beat cycle (Fig. 8). On the downstroke, as the fin's leading edge peels away from the body, fluid on the lateral side of the fin rushes into the gap created between the medial fin surface and the body. As the remainder of the fin is abducted, a trailing vortex bubble is produced, extending from the fin's margin. Sectioning this loop early in its development in the parasagittal plane reveals a free counterclockwise starting vortex (Fig. 8A, *P*1). In accordance with Kelvin's theorem, clockwise bound circulation develops simultaneously, representing the future downstroke stopping vortex. Bound vorticity was not visualized in this study, but can be modeled as an attached leading-edge vortex (Fig. 8A, *a*; see Dickinson and Götz, 1993; Ellington et al., 1996). A free counterclockwise vortex visible in the frontal plane (Fig. 3A; Fig. 8A, *F*1) is consistent with a growing vortex tube. At the end of the downstroke, the initially formed medial leg of the vortex loop has been convected downstream approximately 1–2 fin-chord lengths. Two factors contribute to the early appearance of free clockwise fluid rotation in the wake (as viewed in the parasagittal plane). First, the acceleration reaction (Daniel, 1984) resists deceleration of the pectoral fin at the end of the downstroke and causes entrained fluid to flow from the dorsomedial to the ventrolateral side of the fin. Separation of water at the fin edge results in the rolling-up of negative vorticity (Fig. 8B, *b*). A similar phenomenon is apparent at the end of each half-stroke in the tail wake of swimming fishes (Lighthill, 1975; Triantafyllou and Triantafyllou, 1995), where deceleration of the tail causes fluid to move around the trailing edge and contribute to vortex shedding. Second, clockwise rotation of the fin at the stroke reversal is hypothesized to strengthen bound circulation of the same rotational sense, as demonstrated for insect wing models (Dickinson, 1994). During the fin flip, accumulated bound vorticity (the sum of flows *a* and *b* in Fig. 8B) is forced to the ventrolateral side of the fin and introduced into the wake (see Maxworthy, 1979; Dickinson and Götz, 1996). Thus, by the early stages of stroke reversal, a second free (stopping) vortex is visible in the parasagittal plane (Fig. 3A, lower vortex; Fig. 8C, *P*2).

The general pattern of vortex production on the upstroke mirrors that of the downstroke. As the fin returns towards the body, a clockwise starting vortex is shed from the trailing surface of the fin (Fig. 8D, *P*3) and is matched by a counterclockwise vortex attached at the leading edge (Fig. 8D, *P*4). However, the vortical flow actually visualized in the wake of the upstroke varies directly with swimming speed. For all speeds studied, the downstroke stopping vortex has the same rotational sense as the upstroke starting vortex. A number of kinematic and hydrodynamic factors determine whether these

two vortices are shed as separate discrete structures or a single fused element. The absence of a pause period after the stroke reversal at $0.5\,L\,s^{-1}$ means that *P*3 begins to develop immediately after *P*2 is shed into the wake (Fig. 8D). In this low-speed current (approximately $10\,cm\,s^{-1}$), *P*2 has little time to travel downstream from *P*3, and these vortices therefore remain in close proximity at the beginning of the upstroke. Accordingly, they are predicted to fuse into a single 'stopping–starting' vortex (Fig. 8E, *P*2+*P*3) (Brodsky, 1991, 1994). The combined strength of this free negative circulation counteracts the development of positive bound circulation on the return stroke (by the Wagner effect; see Ellington, 1984a; Dickinson, 1996). Since the upstroke at $0.5\,L\,s^{-1}$ is relatively slow (mean T_u=0.30 s; Fig. 7G), *P*4 vorticity, which was never visualized in our experiments at low speed, is expected to be weak (see Dickinson and Götz, 1996, p. 2102) and thus greatly diminished by that of *P*2+*P*3. At the end of the upstroke, *P*1 and *P*2+*P*3 are the major flow structures visible in the parasagittal plane (Figs 3B, 8E) and, together with flow patterns in perpendicular planes (e.g. Fig. 3B, frontal; Fig. 8E, *F*1, *F*2), reflect the introduction of a single vortex ring into the wake.

Patterns of upstroke vorticity observed at higher swimming speeds can be understood in the light of more rapid and forceful fin beats and an increase in near-fin free-stream velocity. At $1.0\,L\,s^{-1}$, the downstroke period is on average 100 ms shorter than at $0.5\,L\,s^{-1}$ (Fig. 7G). As a result, the downstroke vortex ring self-convects more rapidly away from the pectoral fin. A twofold increase in the velocity of the current of the flow tank passing over the fin further speeds the passage of the wake downstream. Accordingly, clockwise vorticity shed at the stroke reversal (Fig. 9A, *P*2) is hypothesized to travel far enough away from the fin to allow upstroke circulation of the same sign to develop separately (Fig. 9B, *P*3). Mean fin upstroke duration at $1.0\,L\,s^{-1}$ is 20 % shorter than that at $0.5\,L\,s^{-1}$ (Fig. 7G) and is also expected to influence flow patterns in the wake. A faster, and presumably stronger, upstroke should yield a well-developed leading-edge vortex (Fig. 9B, *P*4) which, despite its antagonistic interaction with *P*3, is ultimately shed into the wake (Fig. 9C). The failure of *P*3 to fuse with *P*2 (cf. Fig. 8D,E), and the accompanying reduction in *P*3 circulation, may contribute to the survival of *P*4 and its detection in DPIV flow fields (Fig. 6B). Elevated current velocity at the highest swimming speed, $1.5\,L\,s^{-1}$, should, as at $1.0\,L\,s^{-1}$, promote the shedding of *P*2 and *P*3 as distinct vortices. However, the markedly reduced upstroke period (mean 95 ms shorter than at $1.0\,L\,s^{-1}$, and 79 % of T_d at $1.5\,L\,s^{-1}$; Fig. 7G) appears instead to cause the fusion of these structures into a stopping–starting vortex (Fig. 9E). The augmented magnitude of Γ for *P*2+*P*3 must reduce, but does not annihilate, the opposite-sign Γ of *P*4 (Fig. 9F).

The abrupt deceleration of the fin as it returns to the body at the end of the upstroke will cause the release of remaining bound circulation into the wake. In the light of the observation that the parasagittal plane contains at least three centers of vorticity (Fig. 6B,D), yet only a single vortex pair ultimately appears in the frontal plane (Fig. 6A,C), we conclude that the two vortex rings evident at higher swimming speeds must be linked, rather than discrete. A lateral linkage at $1.0\,L\,s^{-1}$ and a broad ventrolateral linkage at $1.5\,L\,s^{-1}$, as depicted in Fig. 9C and 9F, respectively, are consistent with the experimentally determined orthogonal flow patterns. The absence of a third vortex, with counterclockwise rotation, in the frontal plane implies that the medial leg of the upstroke loop is not fully closed upon itself at the end of the upstroke. In the subsequent kinematic pause period, during which the fin remains adducted against the body, the shed upstroke vortex filament may slide posteriorly along the fish's flank and form a complete loop once downstream of the tail (a similar phenomenon has been hypothesized for *Drosophila melanogaster* flight by Dickinson and Götz, 1996). This hypothesis could be tested by subjecting to DPIV analysis particle images more posteriorly situated than those obtained for this study.

The saltatory kinematics of the pectoral fin stroke (i.e. fin movement interrupted by pause) precludes the formation of a continuous, coupled-chain type of wake proposed for some insect wings (Brodsky, 1991, 1994) and fish tails (Videler, 1993; Rayner, 1995). At the low swimming speed of $0.5\,L\,s^{-1}$, each fin beat results in a single torus containing all large-scale vorticity generated by the fin (Fig. 8). At higher swimming speeds, a linked-pair vortex wake is produced consisting of discrete, double-ring structures shed during each fin stroke (Fig. 9) (cf. 'disconnected chain' of Brodsky, 1991, and 'V-like connected rings' of Grodnitsky and Morozov, 1992, in the wake of insects).

Force balance for aquatic locomotion

Average lift and thrust forces calculated from the wake of the sunfish do not differ significantly from the corresponding resistive forces of body weight and drag (Table 2; Fig. 10). Such a force balance is indeed the expected condition during steady locomotion (Daniel and Webb, 1987; Webb, 1988), but has not been demonstrated previously for swimming animals using empirical data. Attempts to resolve theoretically derived locomotor forces on fishes have met with mixed success (Lighthill, 1971; Magnuson, 1978). The force equilibrium observed for *Lepomis macrochirus* at $0.5\,L\,s^{-1}$ indicates that the DPIV system employed here successfully detects the major vortical structures shed during swimming and allows accurate estimates of the momentum injected into the wake, validating the technique for the study of unsteady aquatic force production. In addition, in the case of *L. macrochirus*, this result allows assessment of the contribution of the pectoral fin to thrust and lift at speeds at which paired-fin forces are out of balance (i.e. at and above $U_{p\text{-}c}$). The relationship between swimming speed and measured force can be interpreted in the light of the changing morphology of the fish's wake. Between 0.5 and $1.0\,L\,s^{-1}$, the approximately fivefold increase in forward thrust (Fig. 7E) is attributed to a second, downstream-facing vortex ring formed on the upstroke (Fig. 6B). The plateauing of thrust at $U_{p\text{-}c}$ is mirrored by the observation that pectoral fin-beat frequency in bluegill sunfish peaks at or near

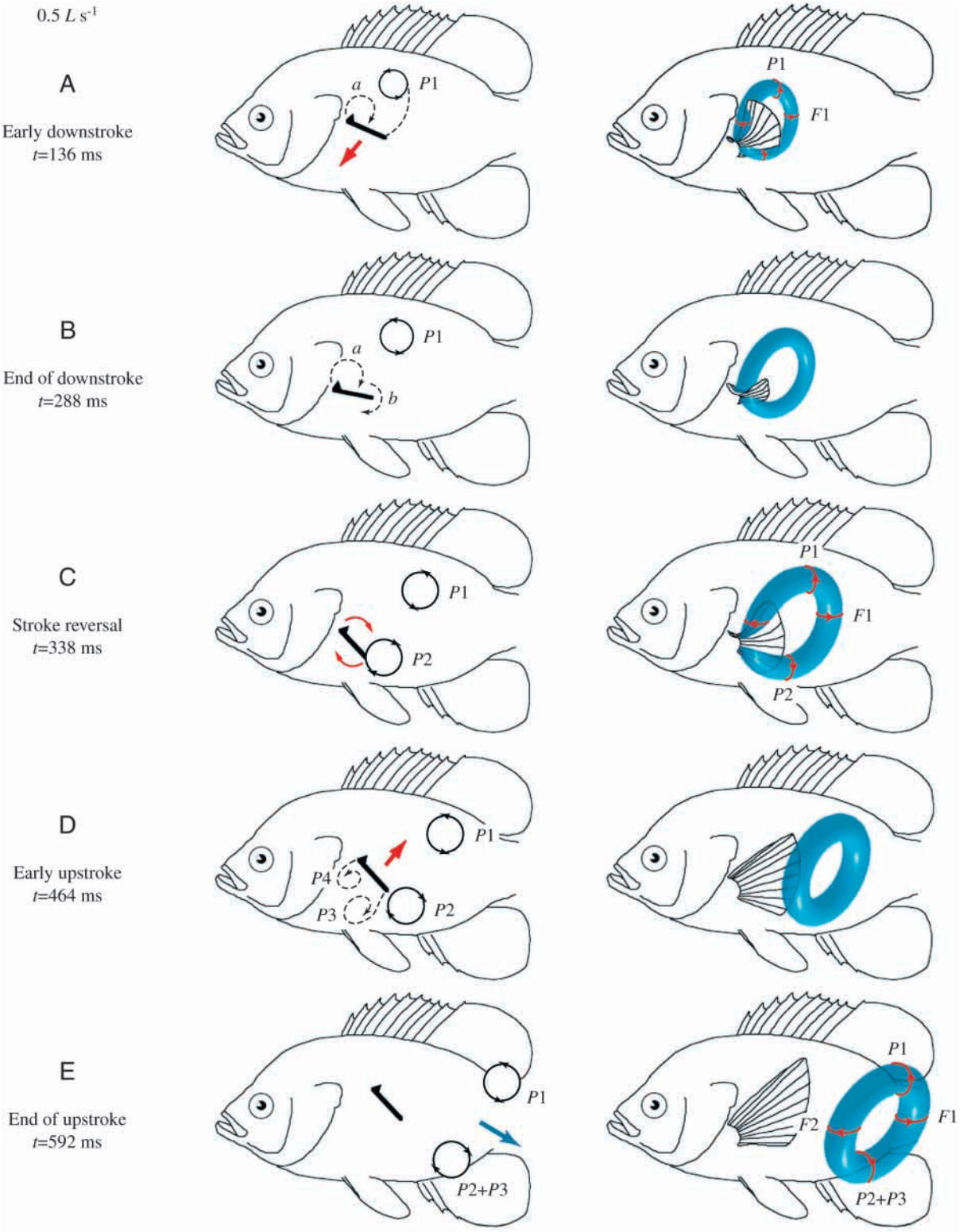

Fig. 8. Formation of the vortex ring wake over the course of the pectoral fin-beat period at $0.5\,L\,s^{-1}$. Left column: proposed mechanism for the development of wake circulation in the parasagittal plane. The pectoral fin is represented as a mid-chordwise section with estimated angles of attack. The triangle at the end of the section marks the dorsal surface of the leading edge. Red arrows indicate the direction of fin movement. Rotational flows visualized using DPIV are represented by black solid-line arrows. Dashed lines indicate predicted flows attached to the fin but not visualized in this study. The blue arrow signifies the orientation of central jet flow observed at the end of the upstroke. All flow structures are shown with the mean free-stream velocity subtracted. See text for discussion of the dynamics of vortex development. Right column: hypothetical three-dimensional reconstructions of fluid flow based on flow patterns observed in perpendicular planar sections of the wake (see Fig. 3). Labelled arrows indicate the direction of measured fluid flow. Each fin-beat cycle results in the introduction of a single, discrete vortex ring with a central fluid jet into the wake. Timings measured from the onset of fin downstroke (t=0). *a*, attached leading-edge vortex; *b*, clockwise flow around fin induced by the acceleration reaction (see text). Other abbreviations as in Figs 4, 6.

the speed of caudal fin recruitment (Gibb et al., 1994; see also Drucker and Jensen, 1996). Downstroke vortex rings at 0.5 and $1.0\,L\,s^{-1}$ exhibit similar jet angles in the parasagittal plane (Figs 4B, 6B), and net lift therefore remains approximately constant (Fig. 7F). The doubling of lift between 1.0 and $1.5\,L\,s^{-1}$ (Fig. 7F) stems directly from the increased tilt of the downstroke ring and its central downwash (Fig. 6D). The generation of additional upward force by the pectoral fins at

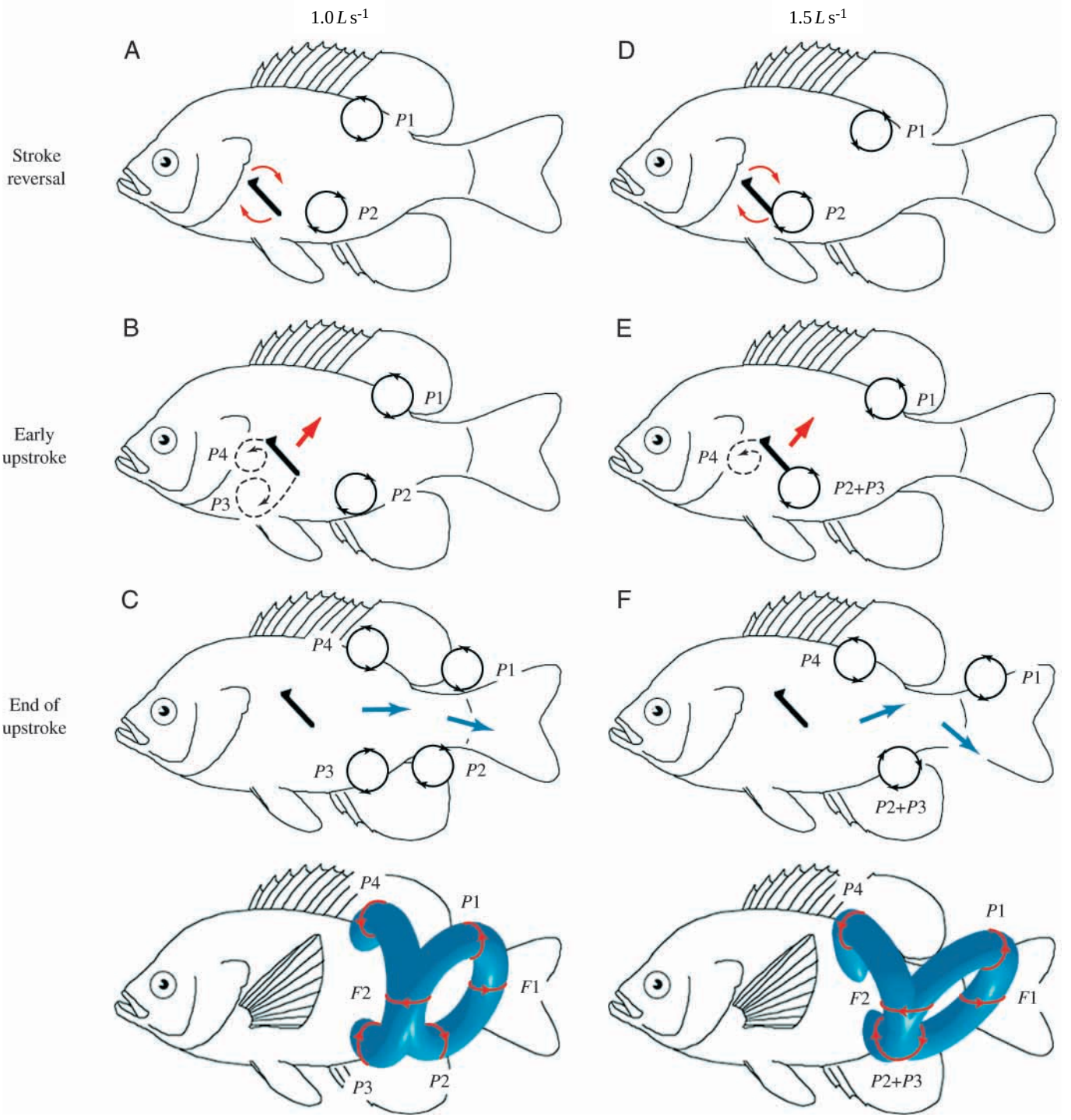

Fig. 9. Development of the linked-pair vortex wake during the second half of the pectoral fin stroke at high swimming speeds. Each column depicts a mechanism by which circulation is generated within the parasagittal plane from the time of stroke reversal to the end of the upstroke (vortex dynamics during the downstroke are similar to that illustrated in Fig. 8A,B). Schematic representations of three-dimensional wake structure, inferred from flow patterns observed in orthogonal planar sections of the wake (Fig. 6), are shown at the bottom. The appearance of 3–4 vortices in the parasagittal plane but only two in the frontal plane indicates the production of linked pairs of vortex rings by each fin during the stroke cycle. With increasing speed, the ring linkage shifts from primarily lateral ($1.0\,L\,s^{-1}$) to ventrolateral ($1.5\,L\,s^{-1}$), thereby altering the orientation of fluid jets and wake forces generated. An explanation of the abbreviations and symbols is given in Fig. 8.

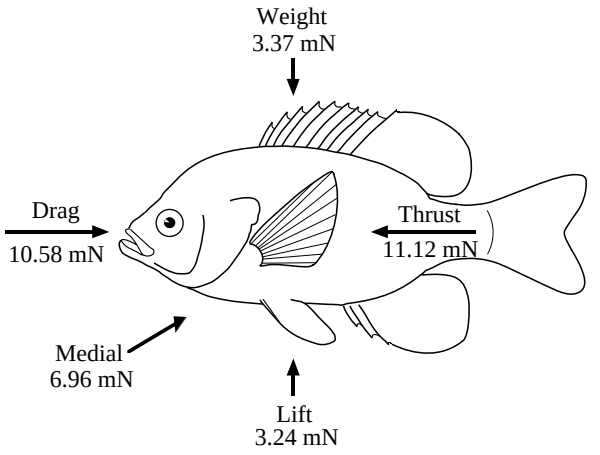

Fig. 10. Summary of empirically determined hydrodynamic force balance on bluegill sunfish swimming at $0.5\,L\,s^{-1}$. Reported thrust and lift values are the mean reaction forces experienced by both left and right pectoral fins together averaged over the fin-stroke period. These propulsive forces calculated from wake velocity data are not significantly different from the measured resistive forces of total body drag and weight (Table 2). A large medially directed reaction force (reported per fin) may be involved in maintaining body stability during locomotion.

high speeds may be necessary to counter the growing negative lift associated with the fish's anterior body profile or positive lift generated posteriorly by oscillation of the tail (Lauder et al., 1996).

A consistent balance of forces computed from wake measurements has been elusive for animals locomoting in fluid. Calculations of lift based on the estimated wake geometry of birds, for example, have often fallen short of values necessary to maintain steady flight against the force of gravity (but see Spedding, 1987). In reconstructing three-dimensional vortex lines in the wake of flying pigeons (*Columba livia*) and jackdaws (*Corvus monedula*), the elegant studies of Spedding et al. (1984) and Spedding (1986) showed that shed vortex rings were paradoxically too small and too weak to provide weight support. Since ring radii measured in orthogonal planar sections of the wake were comparable, the assumption of a more-or-less symmetrical ring is justified. Non-midline and oblique transections of the vortex loop, however, are possible errors that could result in deviations in R and Γ to which calculations of momentum are sensitive. Such types of error are the unavoidable consequence of studying unsteady fluid flows produced by freely moving animals in which the shape, orientation and path of travel of the wake are out of the experimenter's control. For a fish swimming by axial undulation, Müller et al. (1997) recently found that thrust power calculated from flow velocities in frontal-plane transections of the tail's wake exceeded that expected from theory by a factor of three. In this case, circular ring geometry was selected in the absence of complete three-dimensional flow-field information. Since many variations of the vortex ring morphology are theoretically possible from oscillating biofoils (Brodsky, 1994; Rayner, 1995; Dickinson, 1996), the assumption of a particular wake structure based on single-plane views of downstream flow may lead to inaccurate estimations of propulsive force.

For some swimming animals, the locomotor force balance has been proposed to involve an unsteady 'squeeze' mechanism for the supplementation of thrust. Acceleration of the animal's propulsor against the body at the end of the propulsive stroke is thought to eject a rearward jet of water whose reaction provides a forward force (Daniel and Meyhöfer, 1989). This mechanism has been cited for the pectoral fins of fish as a possible means of increasing the total thrust generated per fin beat (Geerlink, 1983). For the bluegill sunfish, however, the pectoral fins are adducted against the body at the end of the upstroke at comparatively low speed. In addition, direct observations of particle motion in the wake of the pectoral fins at the end of the upstroke do not reveal the presence of a strictly downstream-oriented jet (Fig. 3B). For these reasons, we conclude that, for pectoral fin propulsion in sunfish, the squeeze force does not substantially augment thrust produced by vortex ring shedding.

In the present study, locomotor forces were calculated as averages over the course of the fin-stroke duration. Upon completion of the upstroke, remaining bound vorticity is shed from the fin in the form of stopping vortices that migrate away from their starting vortex counterparts (e.g. Fig. 9B,C, *P*3 and *P*4). By the end of the kinematic pause period, free counterrotating vortices are no longer in close proximity. Accordingly, the mutual antagonism of regions of opposite-sign vorticity in the wake, as described by the Wagner effect, is much reduced, and circulation attains its full steady-state magnitude (Dickinson and Götz, 1996, p. 2103). Forces estimated over T are therefore the most informative for resolution of the overall force balance on the animal. However, forces acting on a swimming fish are undoubtedly out of equilibrium at any particular moment during the stride. At high swimming speeds, for example, sunfish generate positive lift on the pectoral fin downstroke and negative lift on the upstroke, as indicated by the tilted orientation of vortex rings in the wake (Fig. 6D). DPIV analysis of flow-field patterns over increasingly small time intervals throughout the fin-beat period would allow estimation of instantaneous locomotor forces (equation 4), a necessary step in determining the time course of force development for labriform swimming.

Comparisons with other animals moving through fluids

Animals locomoting in air must continuously generate lift, a constraint apparent in the form of their wake. For many vertebrates (Kokshaysky, 1979; Spedding et al., 1984; Spedding, 1986) and insects (Grodnitsky and Morozov, 1992, 1993; Dickinson and Götz, 1996), vorticity is shed predominantly on the wing downstroke. Vortex ring momentum angles are quite shallow (e.g. Spedding et al., 1984), reflecting an earthward fluid jet. The upstroke of these animals is thought to perform little or no useful aerodynamic function (Rayner, 1979a; but see Brodsky, 1994; Ellington, 1995). In contrast, buoyant animals swimming in water are

faced with a fundamentally different primary requirement: the production of forward thrust throughout the propulsive cycle. Animals such as the bluegill sunfish that are neutrally buoyant (or nearly so) are freed from the necessity of reserving a large portion of the impulse of each stroke for counteracting the force of gravity. Accordingly, a diversity of mechanisms to supplement thrust may be employed (Daniel and Webb, 1987). The pectoral fin of *Lepomis macrochirus* operates at Reynolds numbers of 4.6×10^3 to 1.4×10^4 between 0.5 and $1.5\,L\,s^{-1}$, values within the range at which the acceleration reaction makes its largest contribution to locomotor force (Webb, 1988). Augmentation of circulation at the end of the downstroke by the rolling up of fluid entrained by the decelerating fin (Fig. 8B, flow *b*) may be characteristic of biological vortex flows in the aquatic medium. For animals moving in the far less dense medium of air, acceleration reaction effects on fluid flow will generally be less pronounced (Daniel and Webb, 1987). At high swimming speeds, *L. macrochirus* sheds vorticity on both half-strokes. The addition of a second vortex ring, with a downstream-facing wash, on the upstroke (Fig. 6B,D) is a further means of increasing force for forward propulsion.

Differences in body and propulsor shape among animals moving through fluids have additional important implications for mechanisms of force production. Unlike most flying birds and insects whose body depth is small compared with wingspan, the bluegill sunfish possesses a deep, laterally compressed body that isolates the relatively short pectoral fins on either side of the animal. This anatomical configuration suggests two hypotheses relevant to the design of fishes for maneuvering. First, a deep body, characteristic of many perciform fishes, may function as a flow barrier to separate the vortex rings generated by the left and right pectoral fins and hence limit their hydrodynamic interactions (Dickinson, 1996). Independent control of the strength and orientation of left- and right-side vortices may be a key factor in allowing rapid, precise turns associated with locomotion in near-shore vegetated habitats or with a planktivorous feeding mode in which frequent changes in body position occur to maintain orientation towards prey. Second, separation of the wake produced by opposite-side fins may confer an advantage in the maintenance of body stability during locomotion. The medially directed force F_z experienced by each fin, contributing neither to lift nor thrust, was unexpectedly large in bluegill, exceeding both mean F_y and F_x per fin (Table 2; Fig. 10). Large, medially oriented reaction forces exerted independently on either side of the animal should assist in stabilizing the body during rectilinear locomotion against rolling moments induced by flow turbulence. Such forces are critical for fishes that are hydrostatically unstable because their center of buoyancy is not located at the center of mass. Even in fishes such as bluegill whose centers of mass and buoyancy coincide (Webb and Weihs, 1994), corrective fin movements generating inward reaction forces are expected in order to offset destabilizing perturbations from local flow.

An additional consequence of the anatomy of swimming fishes is that traditional 'clap and fling' mechanisms cannot function as envisioned for flying animals (Weis-Fogh, 1973). The amplitude of the pectoral fin beat is low compared with the height of the body in virtually all teleost fishes, and the left and right fins therefore do not meet (i.e. clap) at the end of either half-stroke. Fishes whose paired fins do extend below the ventral margin of the body (exemplified by the gar *Lepisosteus* and other basal actinopterygians) or above the dorsal margin (e.g. the butterflyfish *Pantodon*) do not rely on these appendages for propulsion and swim instead primarily by undulation of the trunk and tail. Since hydrodynamic interactions between opposite-side fins are precluded, single vortex loops extending from one side of the fish to the other are unlikely (see Fig. 7A–E in Dickinson, 1996). We predict that the wake of most (if not all) labriform swimmers consists of a series of individual vortex rings (Fig. 8) or linked pairs (Fig. 9) generated separately by each pectoral fin (cf. the 'double chain' wake of Brodsky, 1991).

One role of the clap proposed for flying animals is to destroy stopping vortices shed by both wings and thereby to circumvent inhibition of circulation by the Wagner effect on the return stroke (Ellington, 1984a; Dickinson, 1996). The absence of the pectoral fin clap in fishes may accordingly limit the total circulatory force developed per stroke. Kinematic details of the pectoral fin beat, however, suggest compensatory benefits for thrust production. For instance, the abrupt adduction of the fin against the body at the end of the upstroke should facilitate the rapid transfer of vorticity from propulsor to wake. Additionally, the proximity of each fin to the body at the beginning of the downstroke allows a modified 'fling' in which the wall-like flank serves the same function as a contralateral appendage to augment circulation (Bennett, 1977; Dickinson, 1996). The efficiency of thrust production by labriform swimmers is a function of the non-dimensional Strouhal number (*St*):

$$St = fW/U, \tag{6}$$

where f is fin-beat frequency, W is wake width, taken as the maximal lateral excursion of the pectoral fin tip (see Fig. 8C in Gibb et al., 1994), and U is swimming speed (Triantafyllou et al., 1993). For sunfish, *St* was greatest (mean 0.41) at $0.5\,L\,s^{-1}$ and declined with increasing speed, a pattern noted for the labriform swimmer *Gomphosus varius* by Walker and Westneat (1997). St=0.31 at $1.0\,L\,s^{-1}$ and St=0.20 at $1.5\,L\,s^{-1}$, values within the range at which oscillating hydrofoils are expected to operate with highest propulsive efficiency (Triantafyllou et al., 1993).

The use of DPIV for studies of animal locomotion

In applying digital particle image velocimetry to studies of moving animals, several practical issues need to be addressed. First, it is critical to have control over animal speed and position relative to the laser light sheet. This can be accomplished by using recirculating flumes or wind tunnels, so that animal speed is known, and by using a second camera to quantify the position of the propulsive appendage relative to

the light sheet (Fig. 1). Without knowledge of the location of the propulsor with respect to the flow field, it is impossible to determine what region of the propulsive surface is interacting with the visualized plane of flow. The use of flumes also allows positioning of the animal away from walls and solid surfaces, which can interfere with wake patterns. The study of fish moving in shallow trays, for example, is likely to produce artifactual results due to the close proximity of the bottom of the tank and upper water surface. Second, the use of at least two orthogonal laser plane orientations permits reconstruction of the gross three-dimensional structure of the flow, a task not possible from single-plane analyses alone. The use of three orthogonal laser planes allows flow in three perpendicular directions to be examined and independent estimates of force components to be compared (Table 2). Third, the use of relatively high-speed imaging hardware (greater than 200 fields s^{-1}) allows characterization of the time-dependent nature of biological flow and visualization of the development of vortices around and behind animal appendages. Fourth, the use of automated cross-correlation algorithms for processing particle images yields a complete and evenly spaced matrix of velocity vectors that greatly facilitates calculation of vortex geometry and circulation and removes the uncertainty that arises from tracking individual particles by hand.

Once these practical concerns have been resolved, the applications of DPIV to questions of unsteady biological fluid flow are numerous and represent an exciting area of future research. Assumptions about propulsor shape and kinematics, inherent to mechanical and computational modelling of locomotion (Liu et al., 1996; Van den Berg and Ellington, 1997; Carling et al., 1998), are circumvented by direct flow visualization behind unrestrained animals. Estimation of propulsive force from wake velocity fields both provides insight into the unsteady mechanisms of locomotion and allows calculation of quantities describing locomotor performance. For example, the mechanical efficiency (η) of the pectoral propulsor may be determined as the ratio of forward thrust to total force generated per stride. For *Lepomis macrochirus* swimming at $0.5\,L\,s^{-1}$, η calculated from mean forces pooled across planes (Table 2) was 0.39, a value exceeding the theoretical estimate (0.25) of Blake (1979) for the pectoral fins of angelfish (*Pterophyllum eimekei*). Also of interest for cross-taxonomic comparisons are stride-specific work and power, which can be calculated from wake-derived forces. Over a mean stride length of 0.082 m, the average work performed by the sunfish to swim forward at $0.5\,L\,s^{-1}$ was 0.91 mJ, and the average mechanical power produced by both fins during the stride period was 1.17 mW. Apart from the study of Müller et al. (1997), energetic calculations based upon empirical measurements of the wake of other swimming fishes have yet to be reported.

The DPIV technique further provides an approach for evaluating quantitatively the functional design of propulsive surfaces in organisms moving through fluids. Differences in external shape and patterns of body movement in fishes have long been used for assessment of locomotor design and for reconstruction of the patterns and processes associated with the evolution of locomotor function (Breder, 1926; Affleck, 1950; Gosline, 1971; Thomson and Simanek, 1977). Such indirect assessments can now be coupled with direct measurements of the effects of body form and motion on fluid flow and calculations of the force exerted by animal propulsors.

We thank A. F. Bennett, C. Connon, M. Dickinson, D. Dunn-Rankin, L. Ferry-Graham, A. Gibb, G. Gillis, J. Hicks, R. Josephson, J. Liao, J. Nauen, J. Posner, M. Triantafyllou and C. Wilga for helpful discussions and technical assistance. The manuscript was improved by the comments of two anonymous reviewers. Special thanks to S. Anderson for developing circulation analysis software. Supported by NSF DBI-9750321 to E.G.D. and NSF IBN-9807012 to G.V.L.

References

Affleck, R. J. (1950). Some points in the function, development and evolution of the tail in fishes. *Proc. Zool. Soc. Lond.* **120**, 349–368.

Batchelor, G. K. (1967). *An Introduction to Fluid Mechanics*. Cambridge: Cambridge University Press.

Bennett, L. (1977). Clap and fling aerodynamics – an experimental evaluation. *J. Exp. Biol.* **69**, 261–272.

Blake, R. W. (1979). The mechanics of labriform locomotion. I. Labriform locomotion in the angelfish (*Pterophyllum eimekei*): an analysis of the power stroke. *J. Exp. Biol.* **82**, 255–271.

Blake, R. W. (1983). *Fish Locomotion*. Cambridge: Cambridge University Press.

Breder, C. M., Jr (1926). The locomotion of fishes. *Zoologica* **4**, 159–296.

Brodsky, A. K. (1991). Vortex formation in the tethered flight of the peacock butterfly *Inachis io* L. (Lepidoptera, Nymphalidae) and some aspects of insect flight evolution. *J. Exp. Biol.* **161**, 77–95.

Brodsky, A. K. (1994). *The Evolution of Insect Flight*. Oxford: Oxford University Press.

Carling, J., Bowtell, G. and Williams, T. L. (1994). Swimming in the lamprey: modelling the neural pattern generation, the body dynamics and the fluid mechanics. In *Mechanics and Physiology of Animal Swimming* (ed. L. Maddock, Q. Bone and J. M. V. Rayner), pp. 119–132. Cambridge: Cambridge University Press.

Carling, J., Williams, T. L. and Bowtell, G. (1998). Self-propelled anguilliform swimming: simultaneous solution of the two-dimensional Navier–Stokes equations and Newton's laws of motion. *J. Exp. Biol.* **201**, 3143–3166.

Daniel, T. L. (1984). Unsteady aspects of aquatic locomotion. *Am. Zool.* **24**, 121–134.

Daniel, T. L. and Meyhöfer, E. (1989). Size limits in escape locomotion of carridean shrimp. *J. Exp. Biol.* **143**, 245–265.

Daniel, T. L. and Webb, P. W. (1987). Physical determinants of locomotion. In *Comparative Physiology: Life in Water and on Land* (ed. P. Dejours, L. Bolis, C. R. Taylor and E. R. Weibel), pp. 343–369. Padova: Liviana Press.

Dickinson, M. H. (1994). The effects of wing rotation on unsteady aerodynamic performance at low Reynolds numbers. *J. Exp. Biol.* **192**, 179–206.

Dickinson, M. H. (1996). Unsteady mechanisms of force generation in aquatic and aerial locomotion. *Am. Zool.* **36**, 537–554.

Dickinson, M. H. and Götz, K. G. (1993). Unsteady aerodynamic

performance of model wings at low Reynolds numbers. *J. Exp. Biol.* **174**, 45–64.

Dickinson, M. H. and Götz, K. G. (1996). The wake dynamics and flight forces of the fruit fly *Drosophila melanogaster*. *J. Exp. Biol.* **199**, 2085–2104.

Didden, N. (1979). On the formation of vortex rings: rolling-up and production of circulation. *J. Appl. Math. Physics* **30**, 101–116.

Drucker, E. G. and Jensen, J. S. (1996). Pectoral fin locomotion in the striped surfperch. I. Kinematic effects of swimming speed and body size. *J. Exp. Biol.* **199**, 2235–2242.

Drucker, E. G. and Jensen, J. S. (1997). Kinematic and electromyographic analysis of steady pectoral fin swimming in the surfperches. *J. Exp. Biol.* **200**, 1709–1723.

Ellington, C. P. (1984a). The aerodynamics of hovering insect flight. IV. Aerodynamic mechanisms. *Phil. Trans. R. Soc. Lond. B* **305**, 79–113.

Ellington, C. P. (1984b). The aerodynamics of hovering insect flight. V. A vortex theory. *Phil. Trans. R. Soc. Lond. B* **305**, 115–144.

Ellington, C. P. (1984c). The aerodynamics of hovering insect flight. VI. Lift and power requirements. *Phil. Trans. R. Soc. Lond. B* **305**, 145–181.

Ellington, C. P. (1995). Unsteady aerodynamics of insect flight. In *Biological Fluid Dynamics* (ed. C. P. Ellington and T. J. Pedley), pp. 109–129. Cambridge: Company of Biologists Ltd.

Ellington, C. P., Van den Berg, C., Willmott, A. P. and Thomas, A. L. R. (1996). Leading-edge vortices in insect flight. *Nature* **384**, 626–630.

Fung, Y. C. (1990). *Biomechanics: Motion, Flow, Stress, and Growth*. New York: Springer-Verlag.

Geerlink, P. J. (1983). Pectoral fin kinematics of *Coris formosa* (Teleostei, Labridae). *Neth. J. Zool.* **33**, 515–531.

Gibb, A. C., Jayne, B. C. and Lauder, G. V. (1994). Kinematics of pectoral fin locomotion in the bluegill sunfish *Lepomis macrochirus*. *J. Exp. Biol.* **189**, 133–161.

Gosline, W. A. (1971). *Functional Morphology and Classification of Teleostean Fishes*. Honolulu: University of Hawaii Press.

Grodnitsky, D. L. and Morozov, P. P. (1992). Flow visualization experiments on tethered flying green lacewings *Chrysopa dasyptera*. *J. Exp. Biol.* **169**, 143–163.

Grodnitsky, D. L. and Morozov, P. P. (1993). Vortex formation during tethered flight of functionally and morphologically two-winged insects, including evolutionary considerations on insect flight. *J. Exp. Biol.* **182**, 11–40.

Jayne, B. C. and Lauder, G. V. (1995). Are muscle fibers within fish myotomes activated synchronously? Patterns of recruitment within deep myomeric musculature during swimming in largemouth bass. *J. Exp. Biol.* **198**, 805–815.

Kokshaysky, N. V. (1979). Tracing the wake of a flying bird. *Nature* **279**, 146–148.

Lauder, G. V., Connon, C. and Dunn-Rankin, D. (1996). Visualization of flow behind the tail of swimming fish: new data using DPIV techniques. *Am. Zool.* **36**, 7A.

Lighthill, M. J. (1971). Large-amplitude elongated-body theory of fish locomotion. *Proc. R. Soc. Lond. B* **179**, 125–138.

Lighthill, M. J. (1973). On the Weis-Fogh mechanism of lift generation. *J. Fluid Mech.* **60**, 1–17.

Lighthill, M. J. (1975). *Mathematical Biofluiddynamics*. Philadelphia: Society for Industrial and Applied Mathematics.

Lighthill, M. J. (1986). *An Informal Introduction to Theoretical Fluid Mechanics*. Oxford: Clarendon Press.

Liu, H., Ellington, C. P., Kawachi, K., Van den Berg, C. and Willmott, A. (1998). A computational fluid dynamic study of hawkmoth hovering. *J. Exp. Biol.* **201**, 461–477.

Liu, H., Wassersug, R. J. and Kawachi, K. (1996). A computational fluid dynamics study of tadpole swimming. *J. Exp. Biol.* **199**, 1245–1260.

Liu, H., Wassersug, R. J. and Kawachi, K. (1997). The three-dimensional hydrodynamics of tadpole locomotion. *J. Exp. Biol.* **200**, 2807–2819.

Magnuson, J. J. (1978). Locomotion by scombrid fishes: hydromechanics, morphology, and behavior. In *Fish Physiology*, vol. VII (ed. W. S. Hoar and D. J. Randall), pp. 239–313. New York: Academic Press.

Maxworthy, T. (1972). The structure and stability of vortex rings. *J. Fluid Mech.* **51**, 15–32.

Maxworthy, T. (1977). Some experimental studies of vortex rings. *J. Fluid Mech.* **81**, 465–495.

Maxworthy, T. (1979). Experiments on the Weis-Fogh mechanism of lift generation by insects in hovering flight. Part 1. Dynamics of the 'fling'. *J. Fluid Mech.* **93**, 47–63.

McCutchen, C. W. (1977). Froude propulsive efficiency of a small fish, measured by wake visualization. In *Scale Effects in Animal Locomotion* (ed. T. J. Pedley), pp. 339–363. London: Academic Press.

Milne-Thomson, L. M. (1966). *Theoretical Aerodynamics*, 4th edn. New York: Macmillan.

Müller, U. K., Van den Heuvel, B. L. E., Stamhuis, E. J. and Videler, J. J. (1997). Fish foot prints: morphology and energetics of the wake behind a continuously swimming mullet (*Chelon labrosus* Risso). *J. Exp. Biol.* **200**, 2893–2906.

Raffel, M., Willert, C. E. and Kompenhans, J. (1998). *Particle Image Velocimetry: A Practical Guide*. Heidelberg: Springer-Verlag.

Rayner, J. M. V. (1979a). A new approach to animal flight mechanics. *J. Exp. Biol.* **80**, 17–54.

Rayner, J. M. V. (1979b). A vortex theory of animal flight. Part 1. The vortex wake of a hovering animal. *J. Fluid Mech.* **91**, 697–730.

Rayner, J. M. V. (1995). Dynamics of the vortex wakes of flying and swimming vertebrates. In *Biological Fluid Dynamics* (ed. C. P. Ellington and T. J. Pedley), pp. 131–155. Cambridge: Company of Biologists Ltd.

Rayner, J. M. V., Jones, G. and Thomas, A. (1986). Vortex flow visualizations reveal change in upstroke function with flight speed in bats. *Nature* **321**, 162–164.

Spedding, G. R. (1986). The wake of a jackdaw (*Corvus monedula*) in slow flight. *J. Exp. Biol.* **125**, 287–307.

Spedding, G. R. (1987). The wake of a kestrel (*Falco tinnunculus*) in flapping flight. *J. Exp. Biol.* **127**, 59–78.

Spedding, G. R., Rayner, J. M. V. and Pennycuick, C. J. (1984). Momentum and energy in the wake of a pigeon (*Columba livia*) in slow flight. *J. Exp. Biol.* **111**, 81–102.

Stamhuis, E. J. and Videler, J. J. (1995). Quantitative flow analysis around aquatic animals using laser sheet particle image velocimetry. *J. Exp. Biol.* **198**, 283–294.

Strickler, J. R. (1975). Swimming of planktonic *Cyclops* species (Copepoda, Crustacea): pattern, movements and their control. In *Swimming and Flying in Nature*, vol. 2 (ed. T. Y. Wu, C. J. Brokaw and C. Brennen), pp. 599–613. New York: Plenum Press.

Thomson, K. S. and Simanek, D. E. (1977). Body form and locomotion in sharks. *Am. Zool.* **17**, 343–354.

Triantafyllou, G. S., Triantafyllou, M. S. and Grosenbaugh, M. A. (1993). Optimal thrust development in oscillating foils with application to fish propulsion. *J. Fluids Struct.* **7**, 205–224.

Triantafyllou, M. S. and Triantafyllou, G. S. (1995). An efficient swimming machine. *Scient. Am.* **272**, 64–70.

Van den Berg, C. and Ellington, C. P. (1997). The vortex wake of a 'hovering' model hawkmoth. *Phil. Trans. R. Soc. Lond. B* **352**, 317–328.

Videler, J. J. (1993). *Fish Swimming*. New York: Chapman & Hall.

Vogel, S. (1994). *Life in Moving Fluids: The Physical Biology of Flow*, 2nd edn. Princeton: Princeton University Press.

Vogel, S. and Feder, N. (1966). Visualization of low-speed flow using suspended plastic particles. *Nature* **209**, 186–187.

Walker, J. A. and Westneat, M. W. (1997). Labriform propulsion in fishes: kinematics of flapping aquatic flight in the bird wrasse *Gomphosus varius* (Labridae). *J. Exp. Biol.* **200**, 1549–1569.

Webb, P. W. (1988). Simple physical principles and vertebrate aquatic locomotion. *Am. Zool.* **28**, 709–725.

Webb, P. W. (1993). The effect of solid and porous channel walls on steady swimming of steelhead trout *Oncorhynchus mykiss*. *J. Exp. Biol.* **178**, 97–108.

Webb, P. W. and Blake, R. W. (1985). Swimming. In *Functional Vertebrate Morphology* (ed. M. Hildebrand, D. M. Bramble, K. F. Liem and D. B. Wake), pp. 110–128. Cambridge, MA: Harvard University Press.

Webb, P. W. and Weihs, D. (1994). Hydrostatic stability of fish with swim bladders: not all fish are unstable. *Can. J. Zool.* **72**, 1149–1154.

Weis-Fogh, T. (1973). Quick estimates of flight fitness in hovering animals, including novel mechanisms for lift production. *J. Exp. Biol.* **59**, 169–230.

Westneat, M. W. (1996). Functional morphology of aquatic flight in fishes: kinematics, electromyography, and mechanical modeling of labriform locomotion. *Am. Zool.* **36**, 582–598.

Willert, C. E. and Gharib, M. (1991). Digital particle image velocimetry. *Exp. Fluids* **10**, 181–193.